UNIVERSITY
OF AMSTERDAM

VU UNIVERSITY
AMSTERDAM

Modelling Photovoltaic Silicon-based Luminescent Solar Concentrators with Photon Multiplying Luminophores

Author:
Emil KENSINGTON
12346861 (UvA)

1st Examiner:
Dr. Bruno EHRLER

2nd Examiner:
Prof. Dr. Erik GARNETT

Daily Supervisor:
Benjamin DAIBER

60 ECTS

A thesis submitted in fulfillment of the requirements for an
MSc in Physics and Astronomy, Science for Energy and Sustainability Track

AMOLF physics of
functional complex matter

Hybrid Solar Cells Group
Centre for Nanophotovoltaics, AMOLF

August 26, 2020

Abstract

Modelling Photovoltaic Silicon-based Luminescent Solar Concentrators with Photon Multiplying Luminophores

by Emil KENSINGTON

In this project, we develop and apply a model of a luminescent solar concentrator (LSC) with four photovoltaic silicon (Si) cells attached to its sides. The luminescent molecules of the LSC are varied between a Lumogen 305 dye, a singlet fission tetracene/PbS molecule, and quantum cutting $Yb^{3+} : CsPb(Cl_{1-x}Br_x)_3$ nanocrystals. We subject these three LSCs to a month of real spectral data collected from Denver, Colorado, and observe and compare their performance and behaviour under the varying spectral conditions. The model created is customisable, and allows for further testing and optimisation of nanocrystal-based LSCs in the future.

Acknowledgements

List of Abbreviations

LSC	Luminescent Solar Concentrator
PMMA	Poly(Methyl MethAcrylate)
PLMA	Poly(Lauryl MethAcrylate)
Si	Silicon
NC	Nanocrystals
QD	Quantum Dots
QC	Quantum Cutting
SF	Singlet Fission
PM	Photon Multiplication/Multiplier
PCE	Power Conversion Efficiency
EQE	External Quantum Efficiency
NREL	The National Renewable Energy Laboratory
UV	Ultra Violet
NIR	Near Infrared
APE	Average Photon Energy

Contents

Chapter 1

Introduction

1.1 The Current Climate

As we, here on Earth, experience consecutive seasons of record-setting summer temperatures, the need for action on climate change is becoming more and more apparent. The focus for a means of satisfying our power-hungry societies is shifting towards clean and renewable sources. In particular, photovoltaic applications have been growing dramatically from being unnoticeable on the market just 40 years ago to being a large contributor to renewable electricity now, as shown in Figure 1.1, and are predicted to be dominant in the near future.
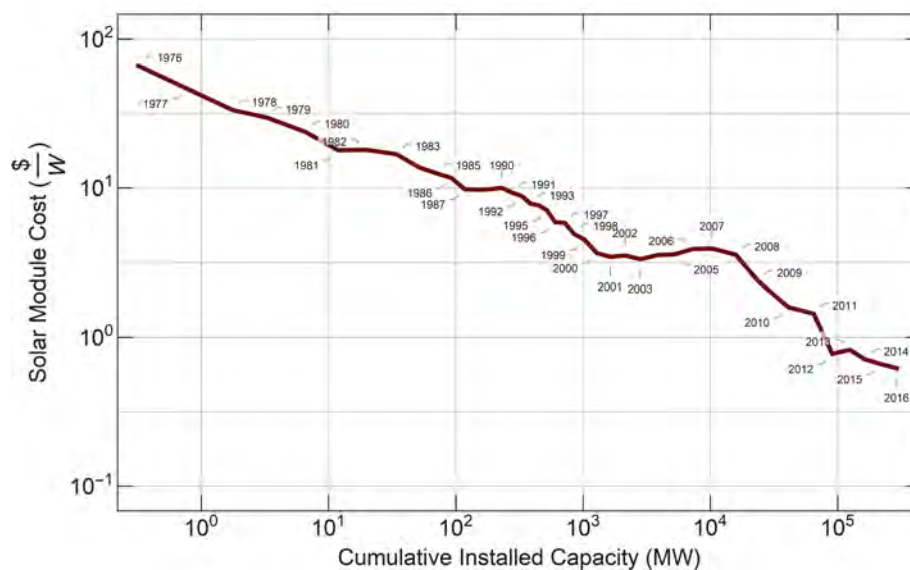
FIGURE 1.1: Logarithmic plot of price of solar modules against the global cumulative installed capacity at peak power, between the years of 1976 to 2016. Data from [1]

Illustrated in Figure 1.1, with the exponential growth in solar applications over the last 40 years has come an exponential decrease in the price of solar modules. For this surge in popularity and energy production of solar panels to continue, we need to continue to look for cheaper and more effective ways to implement the technology. This means utilising all usable spaces and surfaces, and implementing solar cell technologies that best suit that particular location's climate.

Solar concentrating solar panels can be made relatively cheaply, but are commonly very ineffective at absorbing diffuse light [2]. In climates such as those found in Northern Europe, where annual weather is on average cloudy 60% of the time and clear 40% of the time, a solar conversion system should be used that can maximise efficiency in diffuse conditions [3].

1.2   Luminescent Solar Concentrators

A luminescent solar concentrator (LSC) is typically a plastic (PMMA/PLMA - both described further in Section 2.1) film doped with luminophores that re-emit absorbed incident photons from the Sun. Through total internal reflection, the LSC acts as a waveguide for re-emitted photons, carrying them towards solar cells positioned on the sides. An LSC also behaves as a concentrator, effectively concentrating the flux incident on the large top surface of the casing towards the thin solar cells on the sides, allowing for a more efficient collection of diffuse light (sunlight that is scattered by the clouds and sky), all without the need for Sun tracking [4][5][2].

FIGURE 1.2: Photo of an LSC built by UbiQD. The LSC is mostly transparent, with a concentration of the absorbed light directed to the edges, causing them to glow red. Image retrieved, with permission, from UbiQD's Twitter page [6].

LSCs can be built in different shapes, and depending on the build design they can either aim to absorb as much incident irradiance as possible or to transmit a portion of the incident light. This second type extends the application of LSCs into window formats. The bandgap and concentration of the luminophores can be tailored to determine the amount and color of light transmitted, such that the LSC suits the architectural design of the building itself. For tall office buildings with lots of glass, this could constitute a large gain in solar energy from a surface that would otherwise be unused for energy production.

The record LSC efficiency is 7.1%, achieved with an organic dye luminophore and four GaAs cells on the sides, as well as a reflective, light-diffusing coating on the

back [2]. However, improvement is always possible. In order to optimise the design of future LSCs, a realistic working model is crucial.

LSCs are expected to be a very low-cost application of solar cells. The polymeric plastic used is inexpensive, while the more expensive part, the solar cell, is very small and therefore could lead to a big overall reduction in cost.

1.3 Outline of Thesis

The aim of this thesis is to construct a realistic model of a nanocrystal-based LSC with four silicon (Si) solar cells attached to each of the four sides, as illustrated in Figure 2.1. This project is a collaborative project with Tomi Baiki of the Cavendish Laboratory at Cambridge University, UK, and with Benjamin Daiber of the Hybrid Solar Cells Group at AMOLF, NL. This is primarily a computational project, using Wolfram Mathematica software to build and run the simulations. The model is split into three distinct parts - a solar spectra model, an LSC model, and a silicon solar cell model. The LSC model has been constructed by Tomi, while the solar spectra and Si solar cell models are the product of my project at AMOLF.

To model the LSC devices as realistically as possible, we aim to use real measured spectral data from different locations on Earth, allowing us to compare results in different climates. A major benefit of using an LSC compared to a regular concentrating solar cell is that it can concentrate diffuse light. We therefore compare a particularly clear (predominantly direct irradiation) location: Denver, Colorado, and a particularly cloudy (predominantly diffuse irradiation) location: Amsterdam, The Netherlands.

In this thesis, I will first explain the theory behind the models we have built, and the reasoning for why we have chosen to construct it in the way that we have. I will then describe the models, with particular emphasis on the two models I have been involved in making. This is followed by results and a discussion of the behaviour of LSCs, and how they can be improved. I will conclude with the outcome of this research.

Chapter 2

Theory

2.1 Luminescent Solar Concentrators

An LSC has a unique approach to collecting photons emitted from the Sun. The plastic casing doped with luminophores acts as a waveguide to concentrate incident solar photons from the top surface towards thin strips of solar cells on the sides. This process makes it particularly good at converting diffuse irradiation, which is inefficiently used in typical geometrically concentrating solar cell technologies despite being a large portion of total irradiance in many parts of the World, especially in cities and in Europe and Northern Asia. Common concentrators are thermodynamically limited by a factor determined by the materials used. Luminescent solar concentrators (LSCs) navigate around this limit by absorbing and then re-emitting photons, changing their entropy to an extent dictated by the Stokes shift between the absorption and emission of the luminescent material [7].

The photo-conversion processes involved in an LSC can be seen in Figure 2.1. Solar photons (shown in blue) are incident on the large face of the LSC. Immediately a percentage of photons are reflected at the surface - a situation further explained in Figure 2.3. Solar photons that transmit through the air-film interface have the opportunity to either be absorbed by a luminophore embedded in the LSC or to pass straight through and be emitted out the other side. A portion of photons absorbed by the luminophore are emitted at a certain angle relative to the film-air interface that places it within the escape cone; these photons escape the LSC. This is further explained in Figure 2.2. Photons emitted outside of the escape cone are totally internally reflected towards the solar cells positioned on each of the four thin sides, shown in red. In some cases, reabsorption of an emitted photon in another luminophore can occur - a topic investigated in Section 2.3.
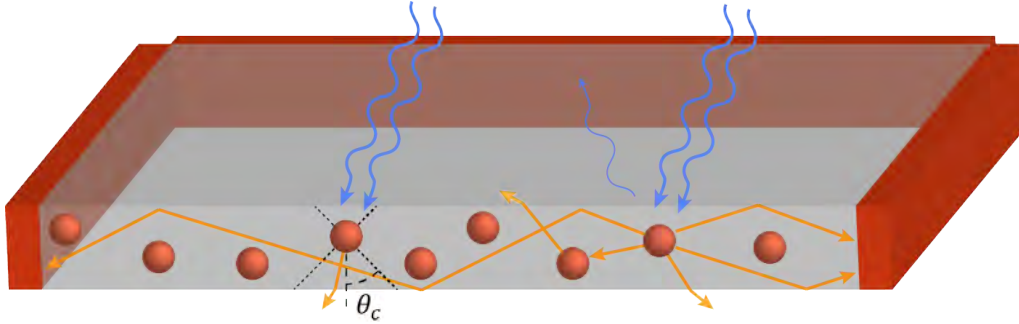
FIGURE 2.1: Schematic cross-section of the nanocrystal-based LSC modelled in this project. Photons (blue arrows) are incident on the surface of the LSC. A small portion are reflected (small blue arrows), while others enter the LSC. Absorption occurs in the luminophore, which then emit photons (orange arrows). Reabsorption can occur as photons are emitted by the luminophores in random directions. Some photons are lost through the escape cone, defined by the critical angle θ_C, while photons emitted outside of the cone are totally internally reflected towards the solar cells (red) positioned on all four sides.

LSCs are commonly fabricated from a polymer plastic matrix such as poly(methyl methacrylate) (PMMA) or poly(lauryl methacrylate) (PLMA). PMMA has many good qualities for use in LSCs, such as being low cost, exhibiting a high resistance to UV-light and other forms of weathering, having excellent optical properties for transmitting light efficiently, having low levels of absorption, and being resistant to changes in temperature [8]. However, PMMA does not mix well with common nanocrystals (NCs), causing them to aggregate.

PLMA has a very different structure to PMMA. It is more well-suited to NC-based LSCs due to interaction between the long LMA carbon chain and the ligands of the NCs creating a very homogeneous dispersion of the NCs [9]. A drawback of PLMA is that it is susceptible to flow, due to being a liquid with a glass transition temperature below room temperature. This issue can be overcome by cross-linking PLMA with ethylene glycol dimethacrylate (EGDMA), however this copolymeric material is not soluble, limiting its use in large-scale solution processing. Both PLMA and PMMA have some absorption of IR photons. Research has been conducted into combining PLMA with PMMA to gain the benefits of each, however in this project we focus on using just PLMA [10].

Redirection of photons towards the solar cells on the sides relies on absorption and re-emission by the doping of luminophores within the plastic. Photons are emitted by the luminophores isotropically, and due to the nature of the film-air interface, total internal reflection only occurs if the angle of incidence of the photon on the interface is above the critical angle relative to the normal, as defined by Snell's law:

$$\theta_C = sin^{-1}\left(\frac{n_1}{n_2}\right). \tag{2.1}$$

As shown in Figure 2.2, the critical angle between the luminophores and each film-air interface forms an "escape cone" with the luminophore in the centre. Any photon emitted from the luminophore at an angle within the cone will transmit across the film-air interface and will be lost. Favoured casing materials such as PMMA and PLMA have a refractive index of $n \approx 1.5$ which characterises a 'trapping efficiency'

- the percentage of photons emitted from a luminophore that are expected to be reflected at the film-air interface rather than transmitted - of $\eta_{TR} = \sqrt{1 - \frac{1}{n^2}} = 75\%$ [10]. The escape cone is an inherent loss in the power conversion efficiency of LSCs, minimised by building the LSC out of a highly refractive material or through further achievement in directional emission from luminophores.
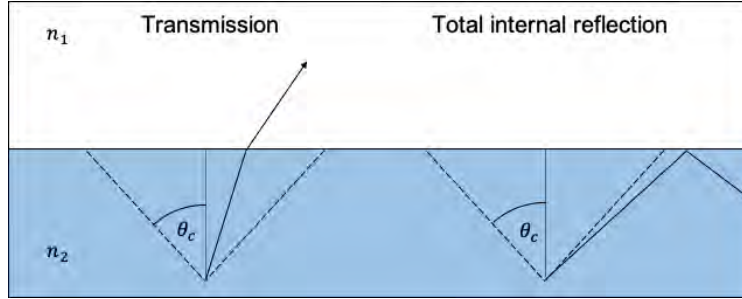

FIGURE 2.2: Diagram of the two possible outcomes of photons emitted from the luminophore interacting with the film-air interface. n_1 is the refractive index of air, n_2 is the refractive index of the film. θ_c is the critical angle, forming an escape cone with the luminophore at the centre. A photon emitted within the escape cone will be transmitted across the interface, while a photon emitted outside of the cone will be internally reflected.

The concentrating effect of LSCs can be understood by looking at the geometry. Incident photons are collected over the large area of the LSC's top surface, $A_{Top} = a * b$. They are then redirected to the long, thin sides where the solar cells reside, area $A_{Side} = b * d$, where a, b and d are the length, width and depth of the LSC. The concentration factor can therefore be calculated with [11]

$$G_C = \frac{A_{Top}}{\#_{Sides} * A_{Side}} = \frac{a * b}{\#_{Sides} * b * d} = \frac{a}{\#_{Sides} * d}. \tag{2.2}$$

This factor is divided by the number of sides ($\#_{Sides}$) containing solar cells to find G_C per cell. During this project we use the dimensions $a = 10$cm, $b = 10$cm, $d = 0.33$cm with $\#_{Sides} = 4$ solar cells giving a concentration factor on each cell of $G_C = 7.5$.

The performance of LSCs are very dependent on the angle of incoming photons. As shown in Figure 2.1, a portion of incident photons are reflected at the surface of the LSC rather than transmitted. The probability of reflection of unpolarised light, such as that from the Sun, is described by Fresnel's equations for parallel and perpendicular (S and P) waves,

$$r_S = \left| \frac{n_1\cos(\theta_i) - n_2\sqrt{1 - (\frac{n_1}{n_2}\sin(\theta_i))^2}}{n_1\cos(\theta_i) + n_2\sqrt{1 - (\frac{n_1}{n_2}\sin(\theta_i))^2}} \right|^2 \tag{2.3}$$

and

$$r_P = \left| \frac{n_1 \sqrt{1 - (\frac{n_1}{n_2} \sin(\theta_i))^2} - n_2\cos(\theta_i)}{n_1 \sqrt{1 - (\frac{n_1}{n_2} \sin(\theta_i))^2} + n_2\cos(\theta_i)} \right|^2 , \tag{2.4}$$

where n_1 and n_2 are the real parts of the refractive indices of air and the LSC material respectively, and θ_i is the angle of incidence. The percentage of photons reflected is calculated as the average of S- and P-wave reflections:

$$\eta_{Refl} = 100 * \frac{1}{2}(r_s + r_p). \tag{2.5}$$

Equation 2.5 is plotted in Figure 2.3 to show the total reflection of unpolarised light at each angle of incidence for an LSC with a refractive index of $n \approx 1.5$.
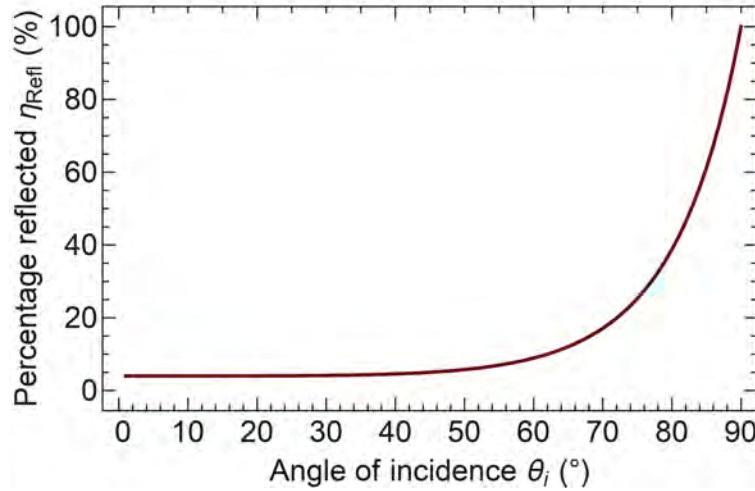

FIGURE 2.3: Plot of the percentage of light reflected at the air-film interface of an LSC with refractive indices $n_1 = 1$ and $n_2 = 1.5$ at each angle of incidence relative to the normal.

As shown in Figure 2.3, at angles above 70° from the normal reflection constitutes a large loss of photons. Angles below this transmit the vast majority of incident photons, with 96% transmission at a normal angle. This is owed to the high refractive index of the plastic casing ($n \approx 1.5$), where lower refractive indices would be more transmissive at sharper incident angles. Due to the reciprocal nature of refractive index boundaries, any photon that enters one side of the LSC will be of a correct angle to escape on the other side. It is therefore key that the photon is absorbed before it reaches the opposite face. Not only does this highlight the importance of having a highly absorbing doping of luminophores, but suggests a peak of the LSC redirecting photons towards the solar cells at higher angles from the normal due to the photons having a longer travel path within the LSC.

As introduced in Section 1.2, an LSC can be designed for use in a window or in an opaque situation. A window LSC has the key function of allowing through a good portion of the visible spectrum so that the device appears transparent. This can be achieved through careful choice of luminophore. Using a low concentration of luminophores could absorb a small percentage of the full light spectrum, while a

luminophore with an absorption bandgap in the ultraviolet (UV) wavelengths and emission in the near infrared (NIR) wavelengths could allow all visible light to pass through undisturbed. A highly absorbing LSC, on the other hand, requires maximum redirectivity. This could stem from using a combination of luminophores to efficiently absorb in the full spectrum of incoming light, as well as a diffuse scattering mirror on the back side of the LSC to redirect photons that would have escaped back into the LSC, increasing their chance of absorption.

2.2 Silicon Semiconductors in Solar Cells

Solar cells rely on semiconducting materials to function. Solar cells based on silicon have become highly stable and highly efficient, owing in part to technological advancements in the makeup of the solar cell itself, but also due to the high capabilities of silicon as a material. Figure 2.4 illustrates the energy structure of inorganic semiconductors such as silicon, which consist of a valence band populated by fully "relaxed" electrons, and a conduction band populated by electrons only after they have been "excited" by an external source of energy, separated by an energy gap named the bandgap. For organic semiconductors such as tetracene the conduction and valence bands are replaced with a LUMO (Lowest Unoccupied Molecular Orbital) and HOMO (Highest Occupied Molecular Orbital) instead, which operate in much the same way as a conduction and valence band.

When a semiconductor is illuminated by a photon of a sufficient energy ($h\nu$), it has the unique effect of exciting a valence-band electron across the band gap and into the conduction band. This process is called generation, and occurs at a rate of G. The conduction band contains many energy levels, but an electron excited to a higher lying energy level by a high-energy photon quickly relaxes back to the band edge, as shown in Figure 2.4. Once in the conduction band, an electron can be attracted by a potential difference through a load to create a current, and is thus called a "charge carrier". When a (negatively charged) electron is excited into the conduction band, it leaves behind a "hole" in the valence band. The pairing of hole and excited electron is called an exciton while they are Coulombically bound. If they are separated by an applied voltage they are no longer an exciton, but a free hole and electron.
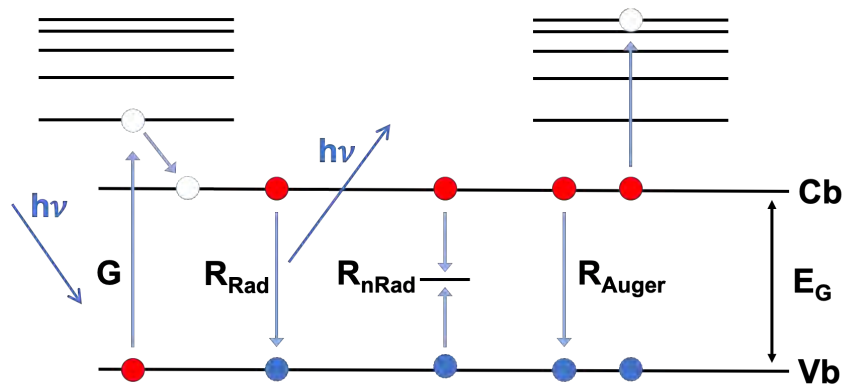
FIGURE 2.4: Simplified diagram of generation and recombination processes in inorganic semiconductors. Red circles represent electrons, and blue, holes. Cb and Vb are the conduction and valence bands, separated by the bandgap energy of the material, E_G. G is the generation rate, and R_{Rad}, R_{nRad}, and R_{Auger} are the radiative, non-radiative (Shockley-Read-Hall), and Auger recombination rates. The arrow on the left indicates an incident photon of energy $h\nu$.

Si has a bandgap of $\approx$ 1.12 eV (1107 nm), meaning it most efficiently absorbs photons at this energy. At higher energies, a quality called the quantum defect becomes apparent due to higher-energy photons exciting the electrons far above the conduction band, which then relax to the band edge, leading to a growing loss in power conversion efficiency. This quantum defect is visualised in Figure 2.5.
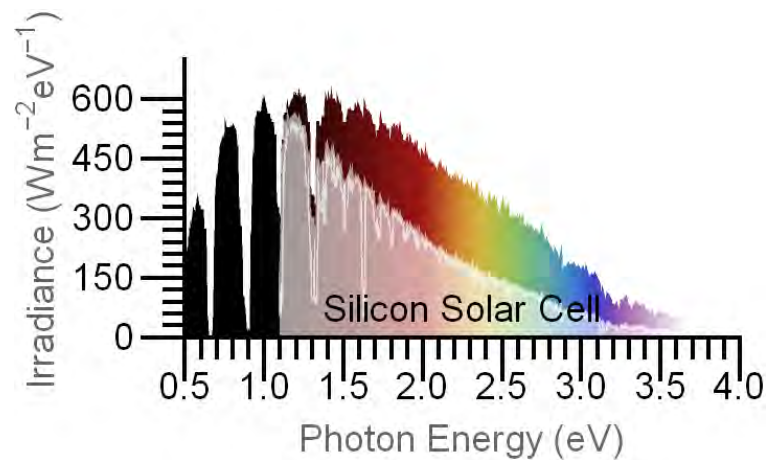
FIGURE 2.5: A comparison between the standard AM1.5G spectrum with the absorption of silicon. The shaded region is the total power absorbed by the silicon. The growing gap in the y-axis between the silicon absorption and the solar spectrum is the quantum defect causing losses of absorbed power due to the size of the silicon bandgap.

The opposite of generation is recombination - the event of an excited electron recombining with a hole down in the valence band. Recombined electrons equate to a loss in current, which lead to an unwanted loss in efficiency. It is therefore essential for an efficient solar cell to lose as few electrons to recombination as possible. Recombination in a semiconductor occurs at a rate of R.

As illustrated in Figure 2.4, recombination occurs in different forms. Radiative recombination (R_{Rad}) is the exact opposite action of generation - an excited electron relaxes across the bandgap, recombining with a hole and emitting a photon of energy $h\nu$ equal to the bandgap energy.

Non-radiative forms of recombination (R_{nRad}) do not emit a photon. For silicon, the dominant form of non-radiative recombination is Shockley-Read-Hall (SRH) recombination. This involves the thermalisation (dissipation of energy through the emission of heat in the form of phonons) of excited electrons through trap states that appear within the bandgap due to defects in the material.

Auger recombination (J_{Auger}) is the process of an electron recombining with a hole, but instead of emitting a photon it gives its energy to an already-excited electron, exciting it further into the conduction band and heating it up, where it then cools and thermalises back down to the band edge. Auger recombination becomes very important in Si solar cells at high carrier concentrations.

Based on these three main forms of charge carrier recombination, a solar cells' behaviour when under varying illumination can be categorised into three separate regimes by analysing Equation 2.6.

$$R_{Eff} = k_1 n + k_2 n^2 + k_3 n^3, \tag{2.6}$$

where $k_{1,2,3}$ are the recombination constants of non-radiative (SRH), radiative and Auger respectively. n is proportional to light intensity, and from this equation we can see that as the intensity increases, the growth of non-radiative recombination is linear, while growth of radiative recombination follows a square law and growth of Auger is a cube law.

n is the total charge carrier density, i.e. the density of excited electrons in the material found by adding intrinsic to excess carriers, $n = n_i + \Delta n$. Excess carriers are electrons that have been photo-excited within the material and are therefore directly proportional to the intensity of the incident light, while intrinsic carriers are already existent in the material.
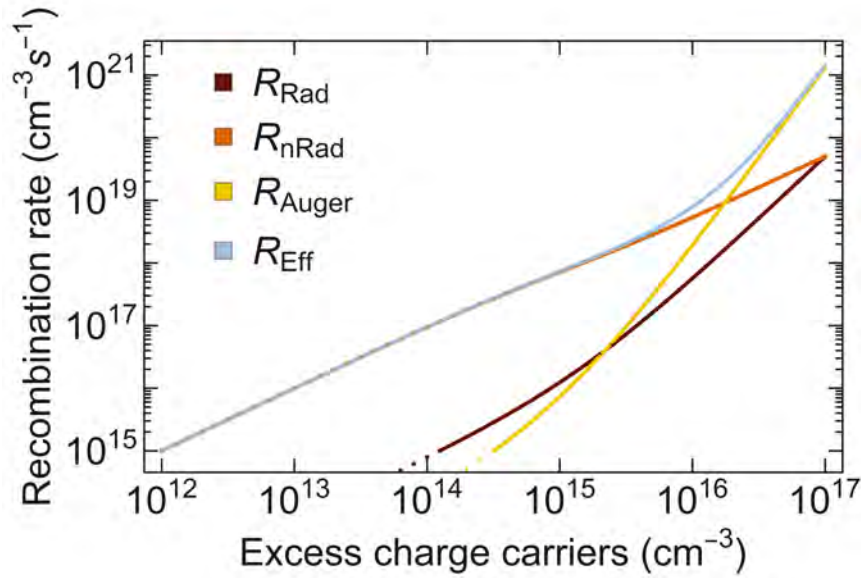
FIGURE 2.6: Graph from the PVLighthouse recombination calculator showing recombination rates including the total effective recombination rate (R_{Eff}) in Si, as excess carrier concentration is increased [12].

For perspective in Figure 2.6, the excess carrier density (Δn) at "one Sun" $\approx 10^{15}\text{cm}^{-3}$. We can therefore see that R_{nRad} is dominant at low light intensities, until between 10 and 15 Suns when Auger recombination becomes dominant, rapidly increasing losses in voltage and current and therefore lowering device efficiency. Using a Si cell for highly concentrating (>10 Suns) devices is therefore ill-advised, however for the LSC model that we have created, we focus on a geometrical concentration factor of 7.5 and so this threshold will not be reached most of the time.

In this project we use a silicon solar cell model based on the record Si solar cell with an efficiency of 26.7% [13]. This efficiency was achieved in a laboratory environment, and so results found using this cell represent an upper limit on the performance we can expect from an LSC coupled with Si cells.

2.3 Luminophores

The purpose of the luminophore in an LSC is to absorb incident photons, and to re-emit them towards the solar cells positioned on the sides of the LSC. The choice of luminophore dictates the effectiveness and behaviour of an LSC and can characterise potentially major losses in the system.

A major loss in efficiency for LSCs in the past has been due to reabsorption of photons by the luminophores. This occurs when the absorption spectrum of the luminophore overlaps the emission spectrum, and so photons emitted have a good chance of being reabsorbed while on their path through the LSC towards the solar cell. Each time a photon is reabsorbed, it is again faced with the aforementioned $100 - \eta_{Tr} = 25\%$ chance of being emitted within the escape cone and not reaching the solar cells. The probability of being lost at some point along the way in n absorption events can be calculated using

$$P_{lost} = 1 - \left(\frac{3}{4}\right)^n. \tag{2.7}$$

For example, if an average of four absorption events occurred, over 68% of photons would be lost versus 25% in a single absorption event (i.e. no reabsorption occurs). Self-reabsorption in luminophores is the primary loss mechanism in early LSCs that functioned on fluorescent dyes and glass concentrators [14][15][16][17]. Since then, many research groups have successfully introduced materials with a large Stokes shift to minimise reabsorption and to allow for a much higher concentration of luminophore and therefore higher amount of directivity of incident photons towards the solar cells [18][10][19]. Two such processes that exhibit this large Stokes shift that are used in this project are singlet fission (SF) and quantum cutting (QC), further described in Sections 2.3.1 and 2.3.2.

In our research we investigate an LSC system using $CsPb(Cl_{1-x}Br_x)_3$ perovskite NCs doped with ytterbium (Yb^{3+}) that absorb a single photon at a tuneable energy of approximately 3.1 eV (400 nm) and emit two photons at 1.24 eV, as well as an LSC with tetracene-PbS NCs that absorb at a singlet energy of around 2.3 eV in the tetracene followed by a broad emission of two triplets by PbS at 0.95 eV (1300 nm). We compare these results to a Lumogen 305 LSC system. The full absorption/emission spectra used in the model can be seen in 3.5.

2.3.1 Quantum cutting NCs

Quantum cutting (QC) is a form of carrier multiplication, where a single high-energy photon is converted into two near-infrared photons. The majority of systems that exhibit QC consist of materials doped with impurity ions, with recent success coming from the lanthanide family (Tb^{3+}, Dy^{3+}, Eu^{3+}, Ce^{3+}, Yb^{3+}). Yb^{3+} is a known activator of QC in bulk crystals, and with an emission energy of 1.24 eV it is very well matched with the 1.12 eV Si bandgap. QC can only occur when the bandgap of the dopant (in our case Yb^{3+}) is less than half that of the host molecule.

Perovskite NCs have become a focus point of luminescent materials due to having a broad range of tuneable bandgap wavelengths, a narrow full width half maxima (FWHM) (<25 nm), and a high PLQY of >70% [20]. Previous studies have successfully used Yb^{3+}-doped $CsPb(Cl_{1-x}Br_x)_3$ to exhibit QC in an LSC setup [21][22]. $CsPb(Cl_{1-x}Br_x)_3$ is a particularly interesting perovskite for this application due to having a bandgap that can be easily tuned across a large range by not only varying quantum confinement, but also by adjusting the ratio of Cl to Br (by changing quantity x) [23]. Yb^{3+}-doped $CsPb(Cl_{1-x}Br_x)_3$ combines the large absorption cross-section and high PLQY of $CsPb(Cl_{1-x}Br_x)_3$ with the long lifetime, narrow emission, and very large Stokes shift of the Yb^{3+} [24][22]. The emission from the dopant has a sharp peak at 990 nm (1.25 eV) and when doped into $CsPb(Cl_{1-x}Br_x)_3$ a photoluminescent quantum yield (PLQY) exceeding 170% has been achieved [24].

Yb^{3+} has a single $^2F_{5/2}$ excited state above the $F_{7/2}$ ground state. An f-f transition is forbidden, meaning the Yb^{3+} instead becomes excited through the absorption of light by the host NCs [25]. The high energy difference between absorption and emission in doped perovskites is made possible by this decoupling between processes. It is thought that the sensitization of Yb^{3+}-doped $CsPbCl_3$ occurs through a defect state induced by the presence of the Yb^{3+}, named a defect complex. This is illustrated in Figure 2.7. We can see here that a trapped excited state is formed, followed

by a nearly resonant energy transfer through a quantum cutting step, producing two Yb^{3+} ions simultaneously [24].
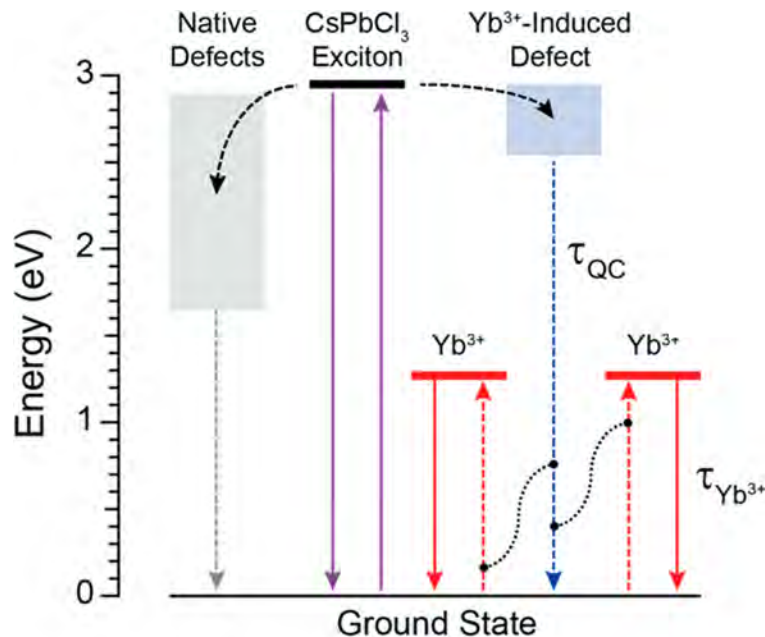

FIGURE 2.7: Proposed energy diagram showing the mechanism of Yb^{3+} sensitisation through a dopant-induced defect state known as a defect complex. Diagram taken from [24].

High concentrations of Yb^{3+} are required to efficiently quench the PL of the host $CsPbCl_3$, as an induced defect must be very close to the $CsPbCl_3$ exciton both energetically and spatially to increase electronic coupling, otherwise $CsPbCl_3$-to-Yb^{3+} energy transfer is very slow [24].

Research has shown that a post-synthetic conversion of Yb^{3+}:$CsPbCl_3$ into Yb^{3+}:$CsPb(Cl_{1-x}Br_x)_3$ is possible without compromising the exceptional PLQY of the Yb^{3+}:$CsPbCl_3$ NCs [23]. By adjusting the ratio of Cl:Br present in the NC, the bandgap can be tuned from 3.06 eV in $CsPbCl_3$ down to 2.53 eV in $CsPb(Cl_{0.25}Br_{0.75})_3$. Levels of Br above this point affect PLQY dramatically due to dropping below the energy threshold for quantum cutting that is twice the bandgap of Yb^{3+}.

As mentioned in Section 2.3, our model uses Yb^{3+}:$CsPb(Cl_{1-x}Br_x)_3$ with a bandgap of 3.1 eV. The absorption of this material can be visualised in Figure 2.8
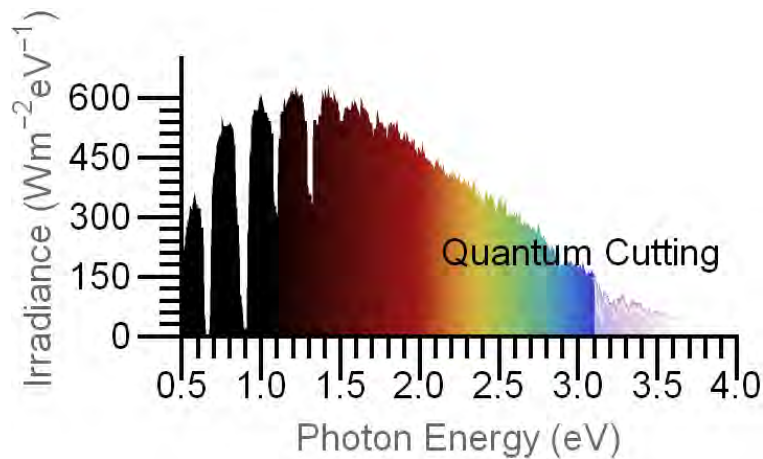
FIGURE 2.8: Absorption spectrum of a quantum cutting material with a bandgap of 3.1 eV.

A material with such a high bandgap is very well suited for a window as they don't absorb the majority of the visible spectrum.

Issues with Yb^{3+}-doped $CsPb(Cl_{1-x}Br_x)_3$

Despite the unique capabilities of Yb^{3+}-doped $CsPb(Cl_{1-x}Br_x)_3$ listed above, there remain issues in LSC systems based on these particular NCs. Most relevant of these for our theoretical calculations is that Yb^{3+} exhibits a long emission lifetime ($\tau_{Avg} \approx 2$ ms)[19]. This, in combination with the large absorption cross-section of $CsPbCl_3$ perovskites, means it is possible to saturate the system when under intense photon flux. Milstein et. al. show in Figure 2.9 that increasing the excitation rate of Yb^{3+}:$CsPbCl_3$ by a factor of ≈ 17 can reduce PLQY from 170% down to 110%. This effect indicates that a non-radiative route for de-excitation is opened when already-excited NCs are subject to further photoexcitation.
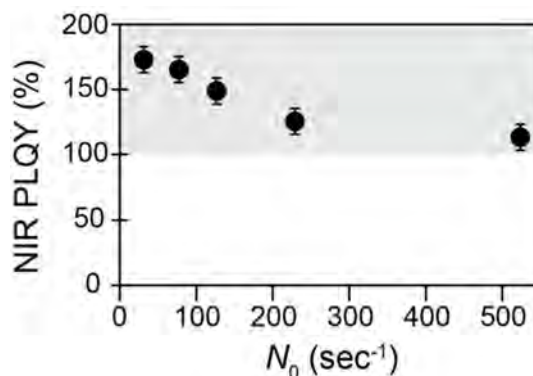
FIGURE 2.9: Relationship of PLQY vs excitation rate (N_0) in Yb^{3+}-doped $CsPbCl_3$. Graph from [24].

Photon flux saturation presents a potential issue when dealing with irradiances of one Sun and above - a situation that is possible depending on location and weather. Erickson et. al. suggest three possibilities for engineering a reduction in the photon flux saturation of quantum cutting crystals: 1) shorten the Yb^{3+} lifetime, 2) decrease excitation rate per Yb^{3+} ion, and 3) reduce the cross-relaxation rate [26]. Erickson

et. al. suggest 1) could be achieved through non-radiative electron transfer directly to, for example, a Si solar cell. LSCs, however, require photon emission from the luminophore for energy transfer to the Si cells, so this may not be improvable here. Erickson et. al. show that increasing the concentration of Yb^{3+} ions reduces saturation via routes 1) and 2) through improving quantum cutting rates relative to Auger cross relaxation rates - an energy transfer process between an excited state NC and excited Yb^{3+} ions that are already in their luminescent $^2F_{5/2}$ state.

2.3.2 Singlet fission NCs

Singlet fission (SF) is a carrier multiplication process observed in organic materials where an exciton in a high-energy singlet excited state (S_1) is converted in to two lower-energy triplet excitons (T_1), theoretically doubling the number of excited charge carriers within a certain wavelength range, as illustrated in Figure 2.10 **a**.

As previously mentioned, excitation of an electron in an inorganic semiconductor pushes an electron from the HOMO to the LUMO of the material, putting it in an excited singlet state. If the material contains a lowest-lying triplet state (E_{T_1}) that is less than half the energy of the exciton's singlet state (E_{S_1}), singlet fission can occur [27]. SF can be a highly efficient carrier multiplication process, owing to exceptionally fast fission rates of <100 fs in materials such as pentacene (Pc) and tetracene (Tc).
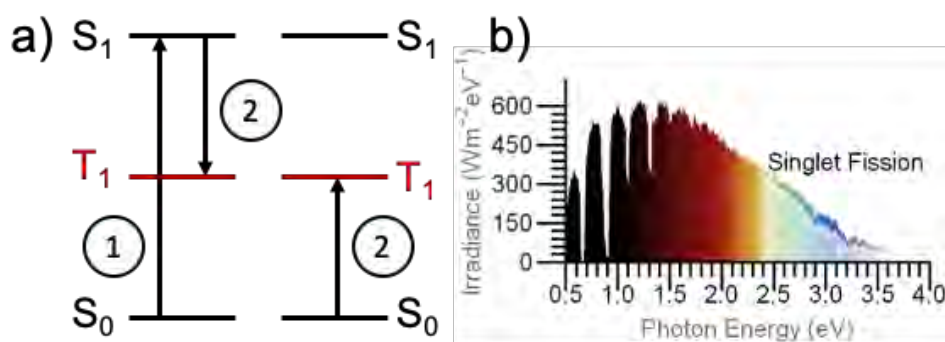

FIGURE 2.10: **a)** Diagram of the singlet fission mechanism. (1) an electron in the donor molecule (left) absorbs energy and moves up to an excited singlet state (S_1). (2) The singlet exciton relaxes to a triplet state (T_1) and transfers half its energy to excite an electron in the acceptor molecule (right) to the T_1 state. Diagram inspired by [28]. **b)** A solar spectrum showing the energy absorbed by a singlet fission material with a bandgap of 2.38 eV.

In a SF-LSC, the SF material has to somehow emit photons for the charge to be transferred to the Si solar cells. The SF process is efficient due to being spin-allowed, however radiative recombination of the triplet states is spin-forbidden and so take a very long time to occur compared to non-radiative routes of recombination in the material, hence reducing photon emission rates and lowering the overall efficiency of the process [29]. For the singlet fission material to more efficiently emit photons towards the solar cells, it can be coupled to a quantum dot (QD) of a different material. The excited triplet state in Tc can transfer to the QDs through an efficient energy transfer process such as Dexter transfer, and once within the QD, radiative recombination and thus emission of a photon can occur.

The efficiency of a photon-multiplying (PM) SF-QD material (η_{PM}) can be calculated through four distinct steps. The efficiency of the singlet fission process (η_{SF}), the efficiency of the triplet diffusion (η_{TD}) from the Tc towards the QDs, the efficiency of triplet transfer (η_{TT}) from the Tc to the QDs, and the efficiency of photoluminescence (η_{PL}) of the NCs [30],

$$\eta_{PM} = \eta_{SF} \times \eta_{TD} \times \eta_{TT} \times \eta_{PL}. \tag{2.8}$$

In an ideal situation, $\eta_{PM} = 200\%$, meaning exactly two photons are emitted for every photon absorbed. In reality, reaching 200% poses a challenge.

PbS QDs have been successfully and efficiently used in SF-QD systems in previous research, with particularly good performance from PbS with a bandgap of 0.93 eV [31][29][30].

Tc exhibits an especially short SF lifetime (<200 ps) relative to its other decay channels, leading to yields close to 200% in Tc films [29][31]. Research by Davis et. al. and Thompson et. al. on PbS NCs with Tc ligands has maximised each efficiency in Equation 2.8 apart from η_{PL}, however they suggest this efficiency can be increased by further optimisation of the NCs themselves through passivation and other techniques [30][31]. The outlook of reaching a near-200% PM efficiency with this combination is optimistic. The emission of the PbS QDs investigated by Davis et. al. (0.96 eV) is below the bandgap of Silicon (Si) (1.12 eV), and so is not ideal, however, the PbS QD's bandgap and therefore emission can be tuned to a more suitable energy by changing its quantum confinement, so long as it remains below half the SF material bandgap for SF to occur.

Issues with Tc:PbS singlet fission nanocrystals

As mentioned, η_{PM} has reached high efficiencies, with the potential for even higher with further NC passivation techniques. However, the conditions for this high efficiency to be reached are very specific. The SF process, as well as triplet diffusion are very sensitive to changes in molecular packing. A high triplet transfer efficiency (η_{TT}) requires a very efficient charge transfer method. Direct charge transfer (DCT) in the form of Dexter charge transfer requires that the Tc molecule lies around 1 nm or less from the PbS NC. This short distance may be difficult to maintain as packing of NCs with Tc is adjusted for optimal triplet diffusion and SF yields [30].

Chapter 3

Models

In this project we implement a series of three separate models that combine to create a full, realistic LSC model. This is split up into a spectra model, an LSC model, and a silicon cell model. In this chapter, I will describe in detail the two models that I have focused on - the spectra and the silicon (Si) solar cell models. I will also summarise the LSC model created by our collaborator Tomi Baiki.

3.1 The Colorado Spectra Model

The solar spectra model uses a year's worth of real spectral data taken from Denver, Colorado. The aim of this model is to manipulate the large quantity of raw spectral data to produce an organised and efficient output of separated direct and diffuse spectra.

3.1.1 The National Renewable Energy Laboratory's Data

The National Renewable Energy Laboratory (NREL) uses a wide range of instruments to collect raw solar and temperature data, as well as other weather data such as wind speeds and air moisture levels. These measurements are taken at the Solar Radiation Research Laboratory (SRRL), based in Denver, Colorado, and the data is uploaded regularly to the Measurement and Instrumentation Data Center (MIDC) [32]. Solar spectra data from a number of different spectroradiometer models can be found on the MIDC, each in one of two setups: global or direct, with direct representing irradiation of photons in a straight line from the sun to the device, and global the sum of direct and all scattered (diffuse) irradiation incident on the device.

3.1.2 Calculating Diffuse Spectra

To model LSC in different atmospheric environments we require direct and diffuse spectral data, as each type interacts differently with the LSC. This is due to direct light coming from a small source in the sky, while diffuse light is spread over the entirety of the hemisphere above the detector.

To calculate the diffuse spectrum from the spectra produced, we can use the equation $Global(\lambda) = Direct(\lambda) * Cos(Zenith) - Diffuse(\lambda)$, rearranged to give the calculation of diffuse irradiance at a given wavelength (λ),

$$\text{Diffuse}(\lambda) = \text{Global}(\lambda) - \text{Direct}(\lambda) \times \text{Cos(Zenith)}. \tag{3.1}$$

The zenith angle represents the angle between the normal to the Earth and the line from the Earth to the Sun. The zenith angle is also published on the MIDC. In this model we assume that the direct spectrum comes from a single, whole angle (i.e. a step size of 1°), while the diffuse spectrum is spread equally from all other incident angles (89° in total). This is not entirely realistic, as there will be brighter and darker spots depending on density of clouds and other objects surrounding the cells, but it is an assumption we must make here as we do not have the data to make it more accurate.

3.1.3   Mathematica Model

A member of our research group has published Si solar cell efficiency results using global spectral data obtained from both Denver, Colorado and from Utrecht, The Netherlands, from the year 2015 [33]. I had the aim to use direct and global spectral data from the same year, 2015, to be able to compare Si cell results with those published previously. For the year 2015, when calculating the diffuse spectra using Equation (3.1), the resulting irradiance drops below $0\frac{W}{m^2}$ for multiple times in the year, as illustrated in Figure 3.1 **a**.
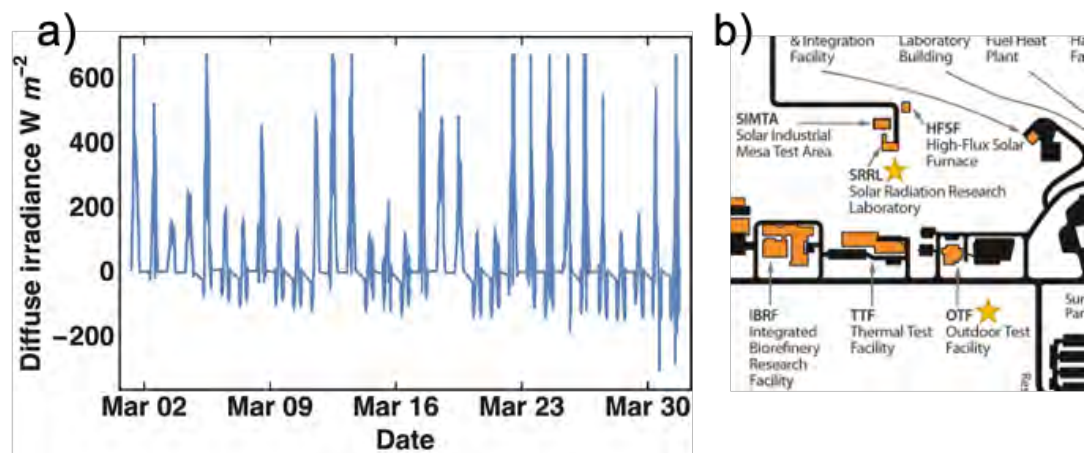

FIGURE 3.1: **a)** Calculated diffuse irradiance over the full month of March 2015, showing many unexpected negative values. **b)** Map of the NREL campus in Denver, Colorado, with gold stars next to the two buildings that the measuring devices used are sited on, over 50m apart.

This issue arises from the locations of the measuring devices being a great distance from each other, shown in Figure 3.1 **b**, leading to a lag in time between changing cloud coverage, for example. A suggestion from Afshin Andreas at NREL was to change to the year 2018 where I could use a different pair of devices that were situated on the same building as one another, just a couple of metres apart. This proved to work very well, as shown in Figure 3.2.
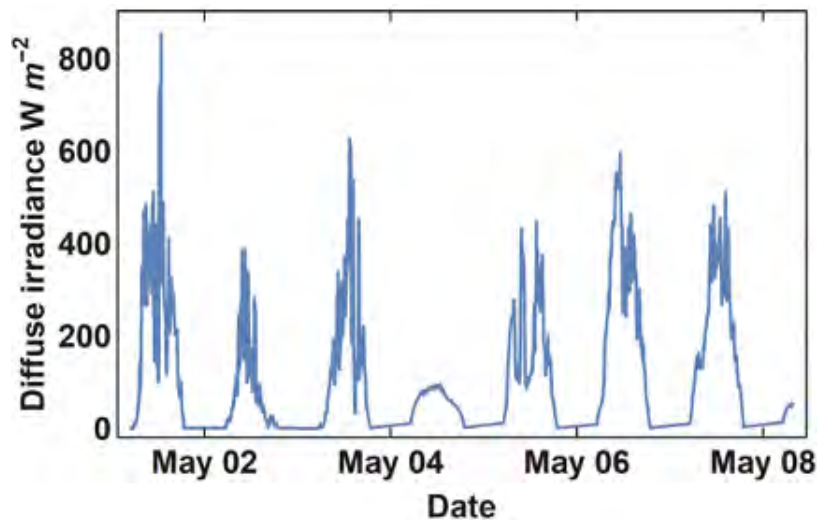
FIGURE 3.2: Diffuse irradiance calculated using the new datasets during the month of May, 2018.

The global measurements are taken by an EKO WISER setup consisting of horizontally mounted MS-711 and MS-712 spectroradiometers. This EKO WISER setup measures a spectral range of 290 nm – 1650 nm. The direct measurements are taken by a PGS-100 (LI-cor-1800) spectroradiometer with a 1-degree field of view, mounted on a Sun-tracker. This silicon-based device measures a spectral range of 350 nm – 1050 nm.

An example of the spectra produced the spectra model can be seen in Figure 3.3. The wavelength range of the spectra has been extended using a fitted blackbody spectrum created for use in a previous model by Futscher et. al., which takes in to account molecular absorption in the Earth's atmosphere [34]. This fit extends the range of the measured and calculated spectra to 280 nm - 4000 nm.
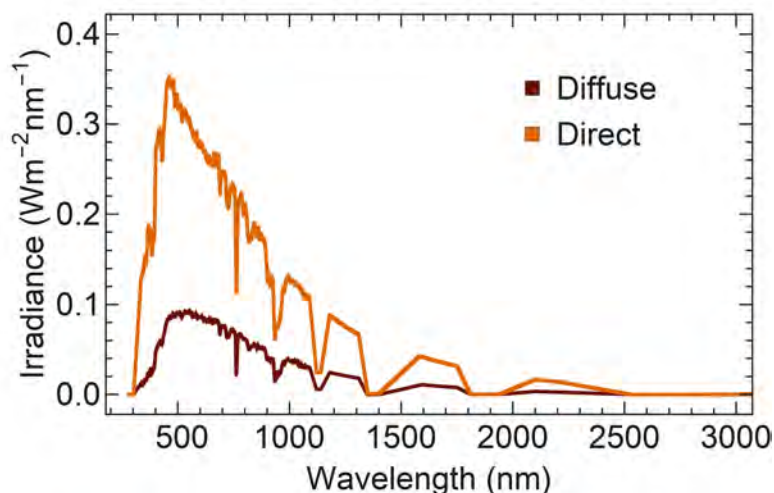

FIGURE 3.3: An example of the direct and diffuse spectra produced by the spectra model, including the blackbody fit.

3.2 The Amsterdam Spectra Model

This section covers a spectra model initially created by Jouke Blum, a BSc student from the Hybrid Solar Cells (HSC) group at AMOLF. This model was extended by Benjamin Daiber, also of the HSC group, for use in our LSC project.

The model uses data collected by a 12-sided light ambience detector (nicknamed the LAD), photographed in Figure 3.4, consisting of an R-G-B spectrometer built into each of its 12 faces. The LAD is situated at the AMOLF solar field, with one of the 12 sides facing south, at the same inclination as a separate south-facing spectroradiometer.

FIGURE 3.4: The 12-sided LAD situated in the solar field at AMOLF. It is encased in a clear, spherical protective plastic shell that is heated to prevent a build-up of condensation.

The aim and outcome of Jouke's project was to build and train a neural network using Wolfram Mathematica software that, using the correct spectral data from the separate spectroradiometer, can create a close estimate of the full spectrum out of the R-G-B readings on the south-facing side of the LAD.

Benjamin took this further by extending the model to estimate a spectrum on each of the other 11 sides, and by adding weightings to each side of the dodecahedron based on the vector in the direction of their normal. This allows us to choose any 3-dimensional angular position around the LAD, and a single spectrum will be produced by the model. We can therefore specify the spectrum at each given angle of incidence, adding to the accuracy of our LSC simulation but sacrificing the ability to follow the behaviour of direct and diffuse spectra separately, as the front face is not Sun-tracking.

3.3 The Luminescent Solar Concentrator Model

This section highlights details regarding the LSC model created by our collaborator Tomi Baiki, of the Cavendish Laboratory, Cambridge University. All the work contained in this section is his.

The LSC model uses a raytracing algorithm to simulate the propagation of photons into and through the LSC, including their interactions with luminophores, the host matrix (PLMA), and film-air boundaries. In this model, the LSC itself is described by a refractive index, n_2, and an absorption spectrum, $A_{LSC}(\lambda)$ in units of cm^{-1}. We simulate three different LSCs based on the following three different luminophores: $Yb^{3+} : CsPb(Cl_{1-x}Br_x)_3$, Lumogen 305, and Tc/PbS. The absorption spectra of each luminophore used, $A_{Luminophore}(\lambda)$, are shown in Figure 3.5 (dashed lines) along with their emission spectra (solid lines). Lumogen 305 is a tried and tested inorganic dye used in LSCs in the past, with strong and broad absorption and emission peaking at just under and above 600 nm, respectively. The $Yb^{3+} : CsPb(Cl_{1-x}Br_x)_3$ and Tc/PbS luminophores are photon-multiplying (PM) materials through quantum cutting and singlet fission processes, respectively. These both have very strong Stokes shifts illustrated by the large gaps between absorption and emission spectra. We assume all absorption in the PM samples occurs in the high bandgap material (Tc and $CsPb(Cl_{1-x}Br_x)_3$ NCs), and all emission in the low-bandgap material (PbS QDs and Yb^{3+} ions).

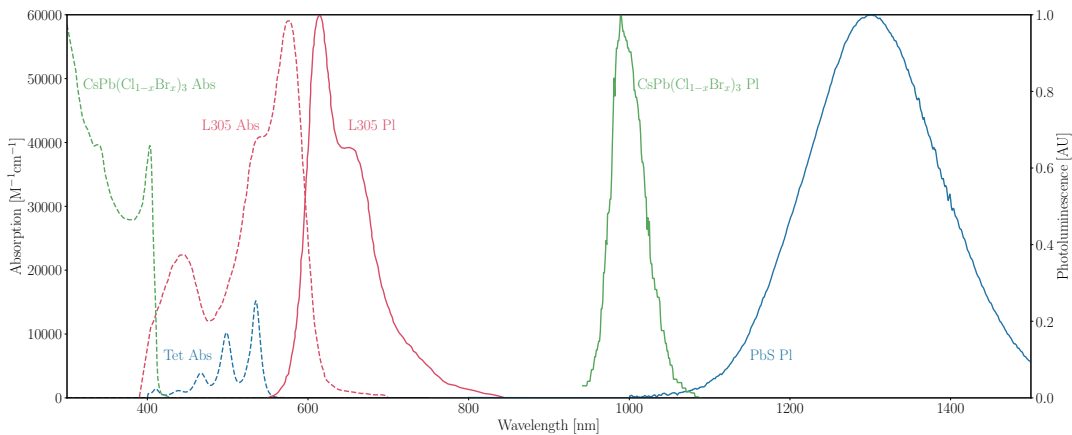FIGURE 3.5: Absorption (dashed lines) and emission (solid lines) spectra of the Tc/PbS (blue) measured by Davis et. al., $Yb^{3+} : CsPb(Cl_{1-x}Br_x)_3$ (green) measured by Gamelin et. al., and Lumogen 305 (red) luminophores used in our simulations [30][24].

For our simulations we have calculated the optimal concentration of each luminophore to maximise absorption while minimising reabsorption. The two materials with large Stokes shifts allow for a very high concentration of 0.1 M for $Yb^{3+} : CsPb(Cl_{1-x}Br_x)_3$ and 0.01 M for Tc/PbS, as they are very insusceptible to reabsorption. Due to the overlap in emission and absorption spectra (see Figure 3.5) of Lumogen 305 there is a peak photon power efficiency at a specific concentration, below which absorption rates are low, and above which reabsorption rates are too high, each leading to a reduction in efficiency. The concentration we have calculated for Lumogen 305 is 0.000001 M.

The model takes 10000 photons at a given wavelength and incident angle, and after

simulating their progression through the LSC, creates a list of wavelengths on each of the four sides. This represents the number of photons and their energies that will arrive at each solar cell.

This model is configurable in many ways such as the luminophore used, the host matrix, the shape, and dimensions of the LSC to allow for optimisation and testing of different materials/setups. A future aim is to compare the performance of each large Stokes shift luminophore-based LSC as photoluminescent quantum efficiency (PLQE) is varied. The PLQE defines the ratio of emitted photons vs incident photons on the luminophore, as shown in Equation 3.2. In some cases it is irradiance dependent, dropping very low at high irradiances, especially for the $Yb^{3+} : CsPb(Cl_{1-x}Br_x)_3$ luminophore. In this model we keep the PLQE constant at either 40%, 80%, 120%, 160%, or 200% across all irradiances and run the simulation for each to determine the minimum PLQE required for a competitive solar cell.

$$PLQE = \frac{\text{Number of photons absorbed}}{\text{Number of photons emitted}}. \tag{3.2}$$

As illustrated in Figure 3.6, the model is built for tracing photons that are incident on the LSC at angles from 1° - 90° from parallel to perpendicular to the face of the LSC (i.e. the x-z plane). When using this model, we therefore must find the absolute angle (θ) of the photon trajectory within this x-z plane. When laid horizontally this is simply the zenith/altitude of the Sun, however calculation of this angle becomes more complicated when the LSC is standing at an arbitrary angle as the azimuthal angle of the Sun also affects its absolute angle.
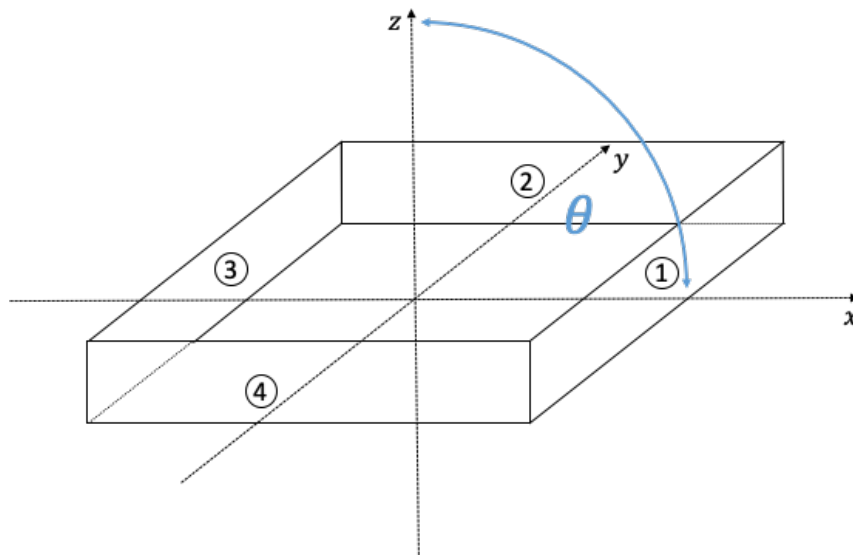

FIGURE 3.6: Diagram of how the angle of incidence (θ) of photons on the LSC is modelled, with the angle ranging across a fixed single plane (x-z plane).

We must also assume in our simulations that, as the horizontal x-axis of the incident-angle plane of photons is in the same direction as an edge of the LSC (side 1 in Figure 3.6), the LSC is always positioned this way relative to the position of the Sun. This is of course an incorrect assumption, as the LSC is static rather than Sun-tracking. For example, if side 1 is South-facing, at dusk and dawn the azimuthal

angle of the Sun would cause photons to be incident from nearer to the corner of the LSC instead of the side. Perhaps this is an assumption with small implications but ideally our model would also include all azimuthal angles of incidence, as variations in performance may occur throughout the day.

3.4 The Silicon Cell Model

The model derived in the following section is an extension of a silicon cell model created for previous publications by Futscher et al. [34][33][27]. This model processes the output of the LSC and applies it to the silicon cell to produce results for the system as a whole, as well as gaining specific outputs for the LSC and Si separately. Data such as current-voltage (J-V) curves, power conversion efficiencies (PCE), and kWh are produced.

In this report we model the current record silicon solar cell, which is a heterojunction interdigitated back contact (HJ-IBC) Si cell, with an efficiency of 26.7% in standard test conditions [13]. To model this specific cell, we use the official external quantum efficiency (EQE) and thickness (L) of the cell (200 micrometres) and subject the cell to standard test conditions[13]. We then fit the current-voltage (J-V) curve to the published results. The original cell made was 180cm^2 in area, and so we assume there is no loss in efficiency after shrinking it down to fit on the thin (≈ 3cm^2) sides of our LSC.

This model builds upon the Shockley-Queisser limit by introducing additional current losses due to non-radiative recombinations such as Shockley-Read-Hall (SRH) recombination, Auger recombination, and parasitic resistances [35]. In our model, the cell is treated as a p-n junction with a quasi-neutral p-type region, a neutral region, and a quasi-neutral n-type region by following the depletion and superposition approximations, as described by Jenny Nelson [33][36]. The depletion approximation supposes that quasi-Fermi levels are constant across the depletion region, the electric field varies linearly across the depletion region while equalling zero in the quasi-neutral regions, and the junction contains no free carriers. The superposition approximation assumes that recombination rates are linear in the neutral regions for minority carrier densities.
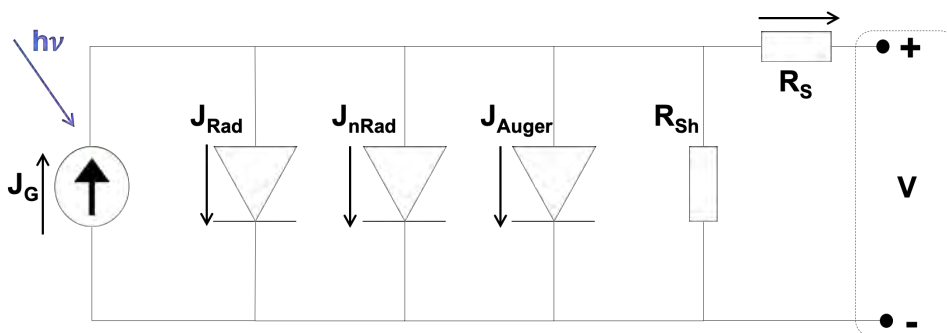

FIGURE 3.7: The equivalent circuit of the Si solar cell model, with black arrows indicating the flow of current. Photons (shown in blue) generate a current (J_G) which is countered by losses through radiative, non-radiative, and Auger recombinations, along with loss from shunt resistance.

Following the work of Jenny Nelson [36], the cell is characterised as a set of diodes, as shown in the equivalent circuit diagram in Figure 3.7, where each form of carrier recombination contributes to a loss in current density, $J(V)$, with units $\frac{A}{m^2}$, at a given voltage, V. The equation,

$$J(V) = J_G(EQE, \Gamma) - J_{Rad}(V, R_S, T)$$
$$- J_{nRad}(V, R_S, T) - J_{Auger}(V, R_S, L, T) - \frac{V + J * R_S}{R_{Sh}} \tag{3.3}$$

describes this relationship, where $J(V)$ is the photo-generated current density, J_{Auger} is the Auger recombination current density, J_{Rad} is the radiative recombination current density, J_{nRad} is non-radiative recombination, and $\frac{v+J*R_S}{R_{Sh}}$ is the current lost due to parasitic shunt resistance (R_{Sh}). These current densities are calculated through diode equations with dependencies on voltage, parasitic series resistance (R_S), temperature (T), and photon flux density (Γ). Equation 3.3 is used to produce a current-voltage relation, thus characterising the behaviour of the cell under different spectral irradiances.
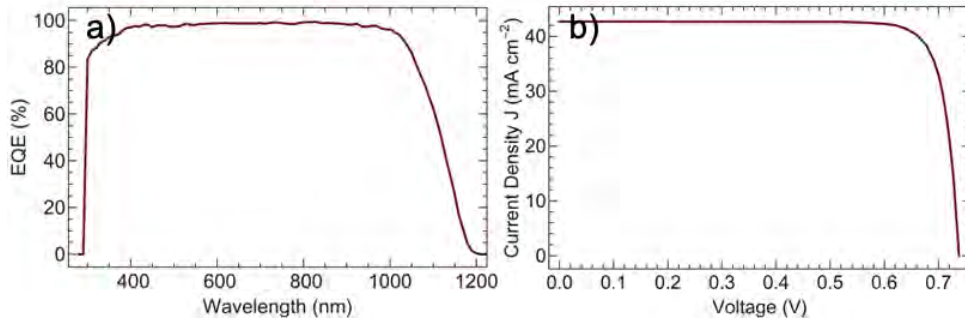

FIGURE 3.8: **a)** The measured external quantum efficiency (*EQE*) of the silicon solar cell used in our simulations. **b)** The measured J-V characteristic of the same silicon cell. [37]

As shown in Equation 3.4, the generated current is found by multiplying the external quantum efficiency per unit energy ($EQE(E)$) of the solar cell by the spectral flux per unit area per unit energy ($\Gamma(E)$). The *EQE* data displayed in Figure 3.8, is taken from the publication of the record cell, and encompasses absorption as well as optical losses such as reflection of the Si cell [37].

$$J_G = q \int_{E_{min}}^{E_{max}} EQE(E) * \Gamma(E) dE, \tag{3.4}$$

with q the elementary charge. J_G can be defined as the total number of charge carriers created in the solar cell before losses occur, multiplied by the unit charge per carrier (q).

In realistic solar cells, however, many different losses occur. The current lost due to radiative recombination is described by the diode equation,

$$J_{Rad} = J_{Rad,0} \left(\exp\left(\frac{V + I * R_S}{k_B T} \right) - 1 \right), \tag{3.5}$$

with

$$J_{Rad,0} = \frac{2\pi q}{c^2 h^3} \int_{E_G}^{E_{max}} \frac{E^2}{\exp\left(\frac{E}{k_B T}\right) - 1} dE \tag{3.6}$$

representing the dark recombination current density. This is a loss that is inherent to the particular semiconducting material used, due to depending only on the temperature and the bandgap of the material (E_G).

SRH recombination is described in Equation 3.7, which occurs through trap states in the material.

$$J_{nRad} = J_{nRad,0} \, n_i(T)^2 \left(\exp\left(\frac{V + J * R_S}{k_B T}\right) - 1\right), \tag{3.7}$$

with $n_i(T)$ the temperature-dependant intrinsic charge carrier density, calculated using Equation 3.10. $J_{nRad,0}$ is the non-radiative recombination constant calculated by

$$J_{nRad,0} = q\left(\frac{D_n}{N_a L_n} + \frac{D_p}{N_d L_p}\right), \tag{3.8}$$

where D_n and D_p are the diffusion constants for electrons and holes, N_a and N_d are the density of acceptor and donor doping densities, and L_n and L_p are the diffusion lengths of electrons and holes respectively. Equation 3.7 reflects that the likelihood of an excited electron relaxing via a trap state increases as diffusion constants increase and diffusion lengths and dopant densities decrease.

Current density lost due to Auger recombination is calculated in the model by

$$J_{Auger} = qLC(T) \, n_i^3 \left(\exp\left(\frac{3(V + IR_S)}{2k_B T}\right) - 1\right), \tag{3.9}$$

where $C(T)$ is the temperature-dependant Auger coefficient, calculated using Equation 3.11.

As mentioned above, parameters such as n_i, C, and E_G are temperature-dependent. These dependencies are calculated in the following equations.

The empirical equation for the temperature-dependence of the intrinsic charge carrier density in Si is

$$n_i = 5.29 * 10^{19} \left(\frac{T}{300K}\right)^{2.54} \exp\left(\frac{-6726}{T}\right) \left[\text{m}^{-3}\right], \tag{3.10}$$

as published by Misiakos and Tsamakis [38].

The Auger coefficient's temperature dependence is calculated using the equation [39]

$$C = 3.79 * 10^{-43} \sqrt{\frac{T}{300}} \left[\frac{\mathrm{m}^6}{\mathrm{s}} \right]. \tag{3.11}$$

The Si bandgap-temperature relation is defined by Varshni's empirical equation [40],

$$E_G = E_{G,0} - \frac{\xi T^2}{T + \chi}, \tag{3.12}$$

with values of $E_{G,0} = 1.17$ eV, $\xi = 4.73 * 10^{-4}$, and $\chi = 636$ K taken from [41].

Equation 3.3 produces an J-V curve, from which we can find the point on the curve at which the cell is operating at its maximum power, named the maximum power point (MPP). We can then calculate the power conversion efficiency of the cell using the equation

$$\eta = 100 * \frac{P_{Out}}{P_{In}}, \tag{3.13}$$

where P_{Out} is the electrical power out of the cell (MPP) and P_{In} is the total spectral irradiance incident on the cell, found by integrating over the full spectrum, i.e. $P_{In} = \int_a^b P(\lambda) d\lambda$, with the boundaries a and b the maximum and minimum wavelength, respectively, in the spectrum and $P(\lambda)$ the power of the spectrum at a given wavelength λ.

With the model defined, it must be fitted to be as accurate as possible under any irradiance. As $J_{nRad,0}$ is a constant reflecting specific details regarding minority carrier diffusion lengths, etc. of the solar cell itself, we treat it as a fitting variable, along with R_S and R_{Sh}. The cell is subjected to AM1.5G radiation at a temperature of 300K, producing a J-V curve. Using Mathematica's NonLinearModelFit function, the fitting parameters within the diode equations are automatically adjusted to produce an accurate replication of the measured device's J-V characteristic, displayed in Figure 3.8 **b**. The fitted values calculated are $R_S = 0.08 \ \Omega\mathrm{cm}^2$, $R_{Sh} = 10000 \ \Omega\mathrm{cm}^2$, and $J_{nRad,0} = 1.88485 * 10^{-42} \mathrm{Am}^4$.

Due to the concentration effect of the LSC, the flux incident on the Si cells has the potential to reach both very low and high intensities, and so the Si model that we use must be capable of accurately handling a broad range of charge carrier densities. Our model can accurately predict behaviour under low and reasonably high illumination without any additional fitting, however at intensities of over ten times one Sun (where one Sun $\approx 1000 \frac{W}{\mathrm{m}^2}$), the code may need to be altered to maintain a realistic behaviour. This is because, as described in Section 2.2, at high intensities Auger recombination becomes the dominant form of recombination and continues to increase at a rapid rate. This behaviour is not accurately reflected in the current model. During this project we have focused on modeling an LSC with only a single layer of luminophores and at a geometrical concentration factor of 7.5 on each solar cell, so intensities are adequately low, but this issue should be monitored in future applications such as in a highly absorbing LSC containing back reflectors and in alternative shapes and dimensions.

The front surface of the silicon cell used in our model is anisotropically etched to minimise reflection, with two layers of dielectric anti-reflection coatings deposited

on top [13]. Literature suggests this is incredibly effective at avoiding reflection from all angles, with the level of reflection remaining fairly constant as angle is increased [42]. Due to this very small variation, we have chosen to not model the angle-dependant reflectivity of the Si cells.

During my project, we are modelling the LSC in a window format. We therefore assume that the temperature (T) is held constant at room temperature ($T = 300$K). When conducting simulations of LSCs positioned outside, temperature within the LSC will be likely to change, and should be taken into account.

3.4.1 Processing the LSC's output

In our LSC setup, we simulate a silicon cell on each of the four sides of the LSC, as shown in Figure 2.1. The Si model is built to work from a power spectrum (Units nm, $\frac{W}{m^2nm}$), as found in typical solar spectra data. However, at each wavelength of light in the spectrum incident on the LSC, and at each angle of incidence, the LSC model produces a simple list of wavelengths that are emitted from the LSC onto each of the four sides where the Si cells reside. Therefore, to combine the Si cells to the LSC simulation, additional steps are required to convert the four output lists of the LSC into four power spectra. A step-by-step process is described in Figure 3.9.

The direct spectrum is incident on the LSC at a single angle - the altitude of the Sun, while the diffuse spectrum is assumed to be incident from all angles (89° in total) equally. In this part of the model I keep the two spectra separate, as they are processed using different methods.

At any given point in time, we have a direct spectrum, a diffuse spectrum, and the altitude of the Sun. Following the process described in Figure 3.9 and its caption, a scaled LSC output power spectrum is created using our spectral data and the many lists output from the LSC simulation. In the case of direct light, step 3 in Figure 3.9 involves totalling over all incident wavelengths, while for diffuse light the LSC output is totalled over all incident wavelengths as well as all incident angles.
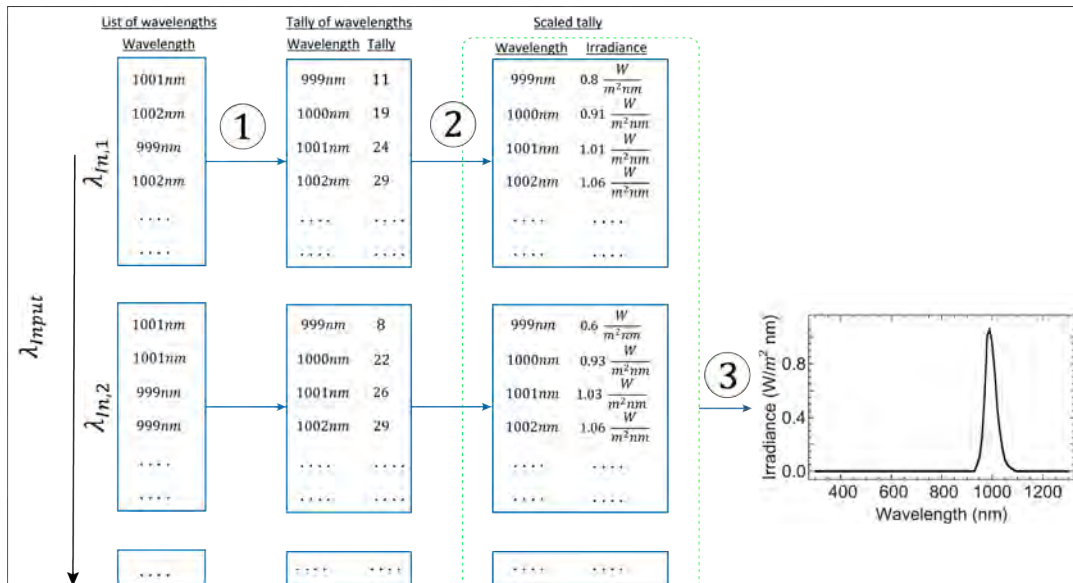
FIGURE 3.9: Diagram showing the spectrum conversion process used in steps (1), (2), and (3), using example data. The first column of boxes contain the raw list of output wavelengths of photons from the LSC on a single side, with each row representing a single wavelength ($\lambda_{In,1}$, for example) of the spectrum incident on the LSC. (1) The Tally function in Mathematica is used to find the total number of photons at each wavelength. This is then sorted by wavelength. (2) The y-axis of this list is then scaled by multiplying the power of the incident spectrum at the specific wavelength $\lambda_{In,x}$ by the ratio of number of photons out to total photons in for each specific output wavelength. (3) A total is taken of all lists contained in the green dashed box, to produce a single, scaled output spectrum as shown.

An extra step in the code was added in the form of an If statement to make up for the fact that the spectral data begins recording only when there is sufficient solar irradiance. This can happen long before sunrise, especially in the Summer months, meaning the altitude of the Sun is below $0°$. For these spectral measurements, when the altitude of the Sun is below 0 degrees, the direct measurements are automatically set to have a flux output of 0, and diffuse light is assumed to be spread equally over $90°$ instead of $89°$.

Chapter 4

Results and Discussion

In this chapter I will present the performance of our luminescent solar concentrator (LSC)/silicon (Si) cell model, compare them to past research, and discuss the causes and implications of our results.

At the time of writing this thesis, we have results for the single month of March, 2018 in Colorado, USA. We have used a single orientation, size and design for our LSC, and have used all three luminophores: Yb^{3+}-doped $CsPb(Cl_{1-x}Br_x)_3$, tetracene (Tc)/PbS, and Lumogen 305. All the data in this section is recorded at 30 minute intervals throughout the daytime in March 2018.

The simulation was run for the entire year of 2018, but an error in the spectral data was noticed too late to correct for inclusion in this thesis, leading to only the month of March being usable.

The photon-multiplying luminophores (Yb^{3+} : $CsPb(Cl_{1-x}Br_x)_3$ and Tc/PbS) are simulated at a constant PLQE of 200%, i.e. exactly two photons emitted for each photon absorbed. The purpose of this is for future simulations to compare the performance of each LSC with PLQEs ranging from 40% to 200%, to find the minimum required to make it competitive with current solar technologies.

As mentioned in Section 3.3, for the quantum cutting (QC) Yb^{3+} : $CsPb(Cl_{1-x}Br_x)_3$- and singlet fission (SF) Tc/PbS-based LSCs in our model we assume that all absorption occurs in the high bandgap material ($CsPb(Cl_{1-x}Br_x)_3$ and Tc) and all emission occurs in the low bandgap material (Yb^{3+} and PbS).

The LSC has dimensions of 10cm x 10cm x $\frac{1}{3}$cm. Using Equation 2.2, the LSC is calculated to have a geometrical concentration factor of $G_C = 7.5$ on each Si solar cell attached to the sides of the LSC.

The LSC was simulated in a horizontal position. As shown in Figure 3.6, Tomi's LSC model is only dependant on angles varying within a single plane perpendicular to the large transmitting face of the LSC. We therefore require only the solar altitude ($90° -$solar zenith angle) as our angle of incidence, as the azimuthal position of the Sun has no effect on the angle in this setup. The incident angles of direct solar irradiance is therefore, on average, closer to the horizontal than the normal, as seen in Section 4.3. This will have a negative effect on direct efficiencies relative to a South-facing and vertically-mounted or typical 40°-incline LSC, as reflection is high at angles very close to horizontal.

A note is that raw spectral measurements are recorded once irradiance is above a certain threshold. This leads to many points early and late in the day where diffuse light is incident on the LSC, but the Sun is actually below the horizon. In these cases

all direct LSC outputs in our model are set to be 0, including efficiencies. The direct spectral measurement devices however experience noise/fluctuations which have lead to varying direct APEs and low direct irradiances even though the Sun was still below the horizon. These points have therefore been removed from all plots of direct measurements in this chapter for clarity.

Temperature in these simulations has been kept constant at room temperature (300K). This is an appropriate assumption for an LSC situated as a window of a building, as it will be heated/cooled by the room temperature inside.

In the following we will investigate the effects of various irradiance conditions on the efficiency of the LSC system.

4.1 Average Photon Energy

The average photon energy (APE) of a spectrum is defined by the energy distribution within it. A high APE indicates the spectrum contains more high-energy blue light, with low APE indicating more red light. For example, the standard solar spectrum, AM1.5G, has an APE of approximately 1.845 eV [34]. The APE metric allows for insights into energy (rather than intensity) dependent behaviour of the solar cell when subjected to varying solar spectra.

The APE is calculated using the equation

$$\text{APE} = \frac{\int_a^b P(\lambda)d\lambda}{q \int_a^b \phi(\lambda)d\lambda}, \tag{4.1}$$

where a and b are the minimum and maximum wavelengths in the spectrum, $P(\lambda)$ is the spectral power per unit wavelength, and $\phi(\lambda)$ the spectral flux per unit wavelength [43]. $\int_a^b P(\lambda)d\lambda$ therefore represents the total photon power in the spectrum, and $\int_a^b \phi(\lambda)d\lambda$ the total photon flux in the spectrum. q is the elementary charge, 1.60218×10^{-19} C. APE is measured in electron volts (eV).

Figures 4.1 and 4.2 show how the efficiency of the PLQE= 200%, Yb^{3+} :
$CsPb(Cl_{1-x}Br_x)_3$-based LSC varies with the APE of the incident diffuse and direct solar spectra, respectively. We can see clearly that at lower APEs, the LSC photon power efficiency is drastically lower than for higher spectral APEs. This is understandable when considering that the onset of absorption for the $CsPb(Cl_{1-x}Br_x)_3$ perovskite is at very high energies (>3 eV). A high APE will have a larger percentage of its photons located at higher energies, leading to a more efficient overall absorption in the LSC.

Photon power efficiency is the ratio of total spectral power out of the thin sides of the LSC where the Si cells are located. It is calculated using Equation 3.13, with $P_{Out} = \int_a^b P_{LSC}(\lambda)d\lambda$ the total spectral LSC output power and $P_{In} = \int_a^b P(\lambda)d\lambda$ the total solar spectral power incident on the LSC.
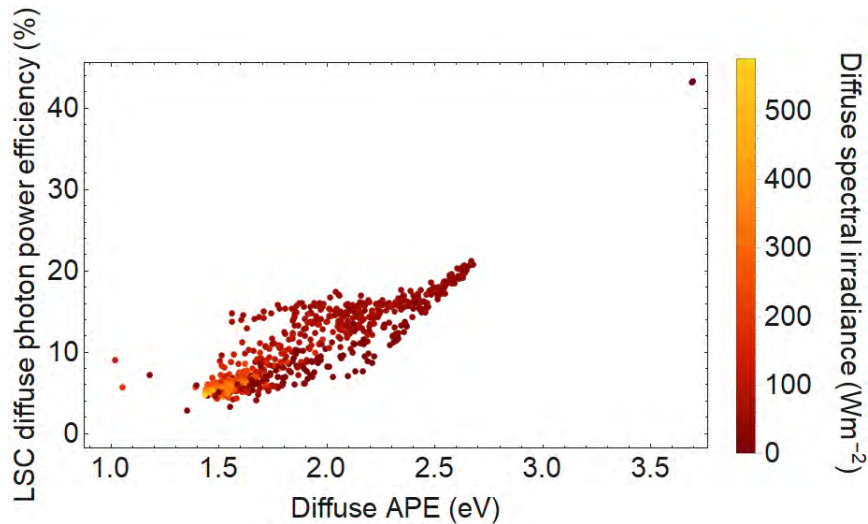
FIGURE 4.1: PLQE=200%, Yb^{3+} : $CsPb(Cl_{1-x}Br_x)_3$ LSC photon power efficiency related to the spectral APE for diffuse irradiation. The points are coloured depending on the total diffuse spectral irradiance.

When comparing the results of the diffuse spectra in Figure 4.1 to the direct spectra in Figure 4.2, we clearly measure more diffuse APEs at high energies (e.g. above 2 eV) than direct. As noted by Debije et. al., this is evidence of the atmospheric phenomenon of high energy photons being scattered by clouds and water vapour in the sky, which leads to the sky around the Sun appearing to be blue [5]. As the diffuse spectra contain predominantly blue photons relative to direct spectra, we see an overall higher conversion efficiency for diffuse light. Also linked to this scattering effect, when looking at the diffuse data, we see that higher irradiances have an overall lower energy and hence have a lower efficiency. Higher rates of scattering not only leads to more blue light, but also a lower irradiance due to extra absorption in the atmosphere.
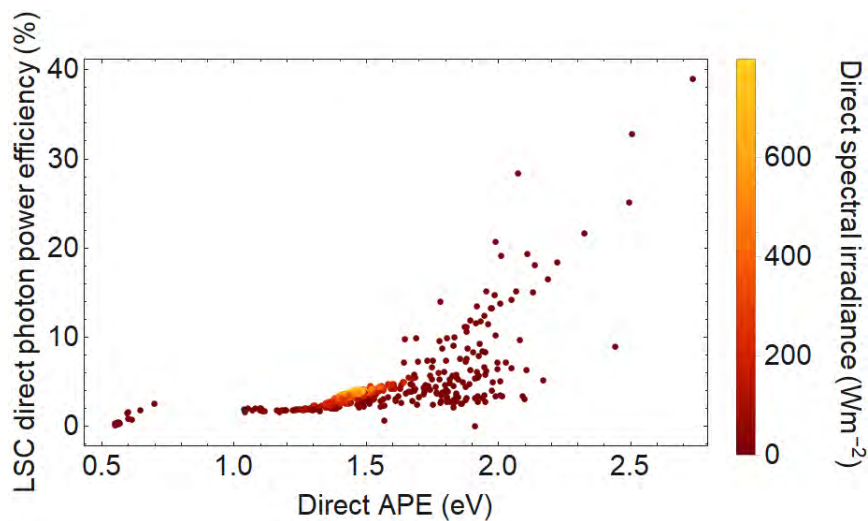

FIGURE 4.2: PLQE=200%, Yb^{3+} : $CsPb(Cl_{1-x}Br_x)_3$ LSC photon power efficiency related to the spectral APE for direct irradiation. The points are coloured depending on the total direct spectral irradiance.

It appears that at very low irradiances, APE is more likely to move to more extreme values, presumably at dusk and dawn when extra absorption and scattering in the atmosphere occurs, thus affecting efficiency drastically for those points.

The range of APEs for direct light is far more concentrated between 1 eV and 2 eV than for diffuse spectra. The dependence of photon power efficiency on APE is also very flat, i.e. very little increase in efficiency as APE is raised. This is due to the very high bandgap of the $CsPb(Cl_{1-x}Br_x)_3$ perovskite, which leaves the system inefficient and insensitive to changes at very low spectral APEs. This also explains the apparent positive acceleration of diffuse efficiencies as diffuse APE approaches high energies.
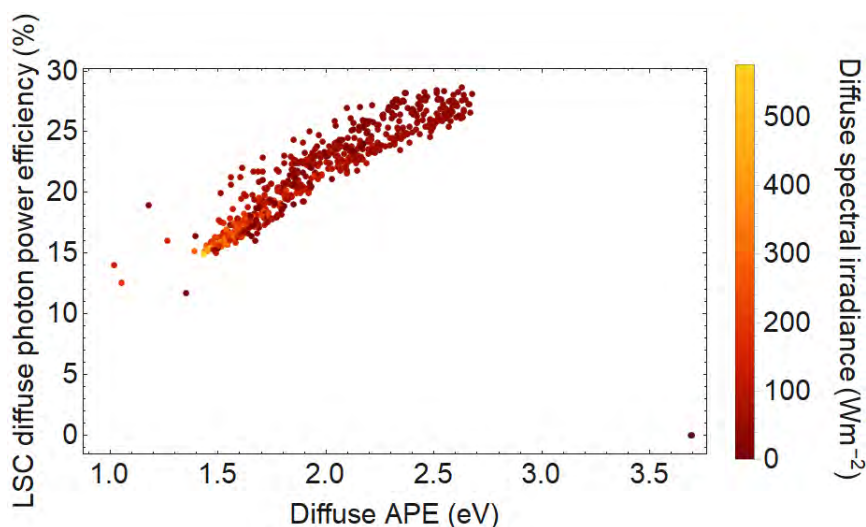

FIGURE 4.3: Tc/PbS LSC photon power efficiency related to the spectral APE for diffuse irradiation. The points are coloured depending on the total diffuse spectral irradiance.

The Tc/PbS (Figure 4.3) and Lumogen 305 (Figure A.3)-based LSCs share many of the same characteristics as the $Yb^{3+} : CsPb(Cl_{1-x}Br_x)_3$-based LSC under diffuse irradiation, however they both have a more consistent gradient of gaining diffuse photon power efficiency with increased spectral APE. Both Tc and Lumogen 305 have absorption onsets that are relatively low, meaning the efficiency is already sensitive to increases in APE at much lower APEs than for the $CsPb(Cl_{1-x}Br_x)_3$ luminophore. This is also reflected in the direct results (Figures 4.4 and A.4) which show much higher photon power efficiencies than the $Yb^{3+} : CsPb(Cl_{1-x}Br_x)_3$ LSC. We can more clearly see in these figures that at a given APE, high direct irradiances have a higher conversion efficiency. High irradiances are most likely to be occuring around midday when the solar altitude is at its highest, at which point reflection at the air-film boundary of the LSC is at a minimum.
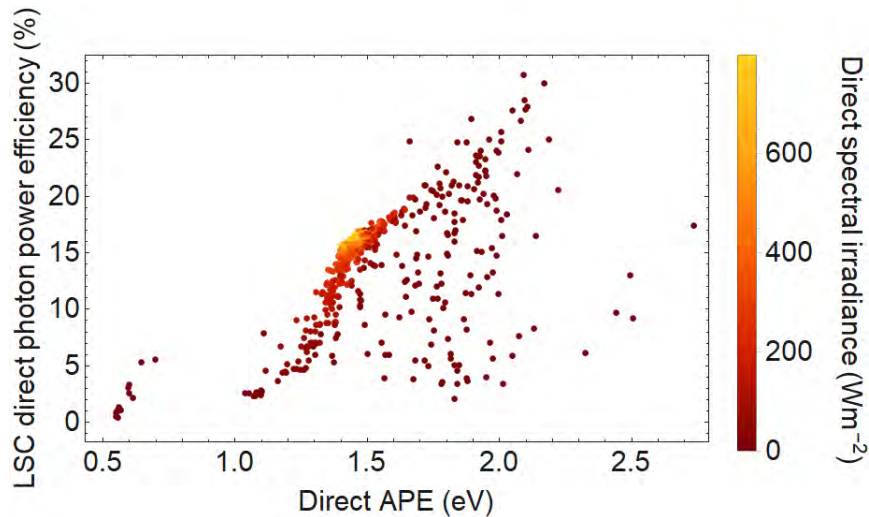
FIGURE 4.4: Tc/PbS LSC photon power efficiency related to the spectral APE for direct irradiation. The points are coloured depending on the total direct spectral irradiance.

4.2 Irradiance Dependence

Figure 4.5 shows the dependency of the $Yb^{3+} : CsPb(Cl_{1-x}Br_x)_3$ LSC with PLQE = 200%'s photon power efficiency and optical efficiency on spectral irradiance.
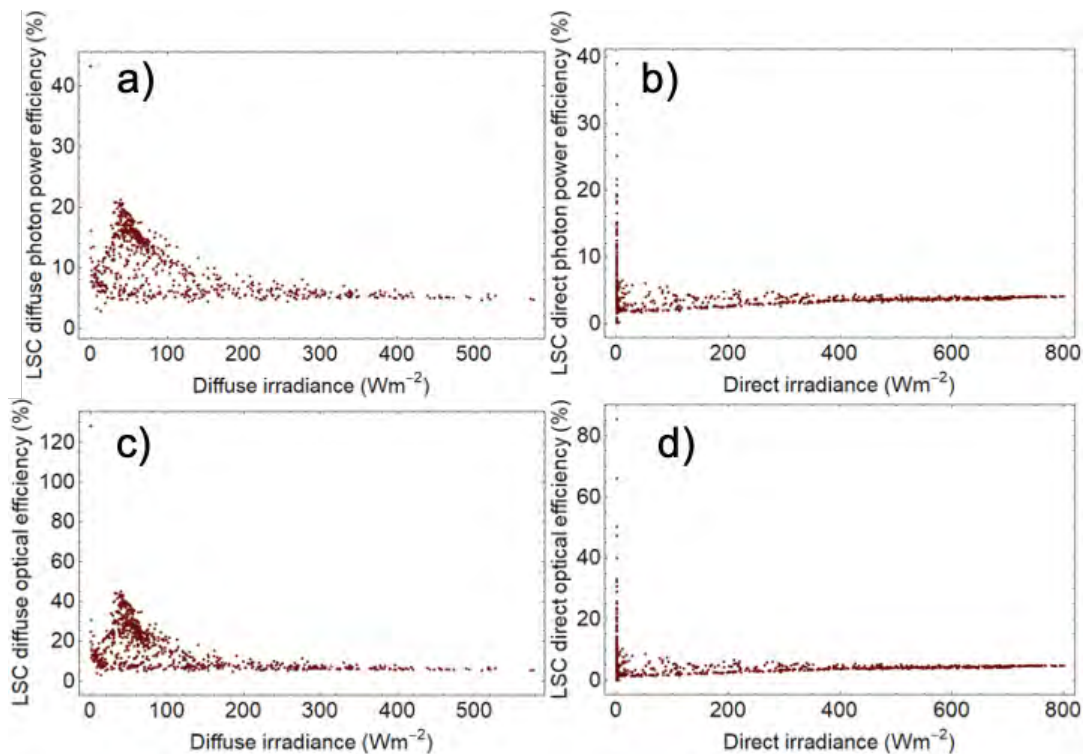

FIGURE 4.5: PLQE = 200%, $Yb^{3+} : CsPb(Cl_{1-x}Br_x)_3$ LSC - plots of **a** diffuse and **b** direct photon power efficiency vs spectral irradiance, and **c** diffuse and **d** direct optical efficiency vs spectral irradiance.

Looking at the diffuse data shown in Figure 4.5 **a** we can see that the LSC's photon power efficiency remains stable at around 5% for high irradiances, while at low irradiance efficiencies vary, mostly increasing above 5% efficiency with very few points dropping below 4%. This may link with the previous statement that a lower irradiance coincides with a higher diffuse APE on cloudy days, leading to a higher absorption efficiency in the high-bandgap luminophores. The stable efficiency across varying irradiance is reflected in the direct data, shown in Figure 4.5 **b**.
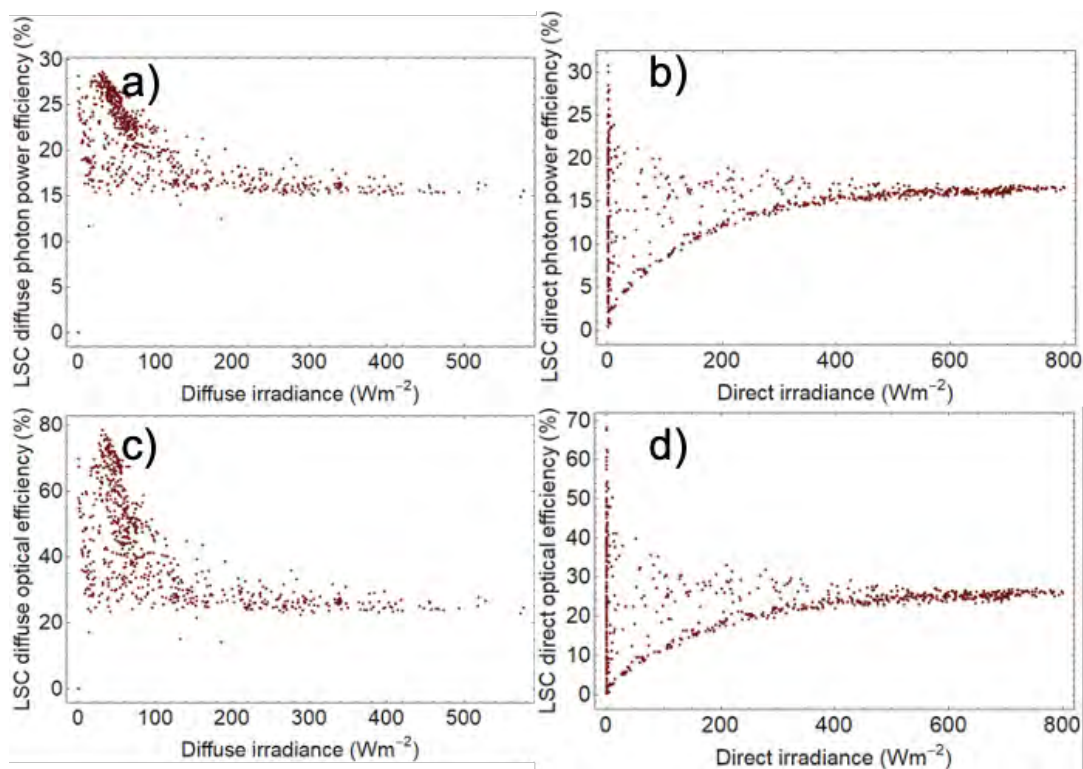

FIGURE 4.6: PLQE = 200%, Tc/PbS LSC - plots of **a** diffuse and **b** direct photon power efficiency vs spectral irradiance, and **c** diffuse and **d** direct optical efficiency vs spectral irradiance.

The direct Yb^{3+} : $CsPb(Cl_{1-x}Br_x)_3$ plot in Figure 4.5 **b** shows a very compact y-axis distribution with overall low efficiencies, especially when compared with the Tc/PbS and Lumogen 305 LSCs in Figures 4.6 **b** and 4.7 **b** respectively. This limited variance and low efficiency will be largely due to the very high absorption bandgap of the $CsPb(Cl_{1-x}Br_x)_3$ of around 3 eV.

As mentioned in Section 4.1, lower diffuse irradiance can occur due to a lower overall irradiance, or because of thicker cloud coverage which leads to bluer light and a higher APE spectra. This then generates higher diffuse efficiencies in the LSC, as seen in the diffuse data in Figures 4.5 **a**, 4.7 **a**, and 4.6 **a**.

The direct Tc/PbS and Lumogen 305 results show a majority of points increasing to a limit of around 16% and 14% in efficiency, respectively, as irradiance increases. This follows the typical, gradual increase and decrease in irradiation as the Sun rises and sets each day, leading to lower angles of incidence and therefore higher amounts of reflection. This is further discussed in Section 4.3.
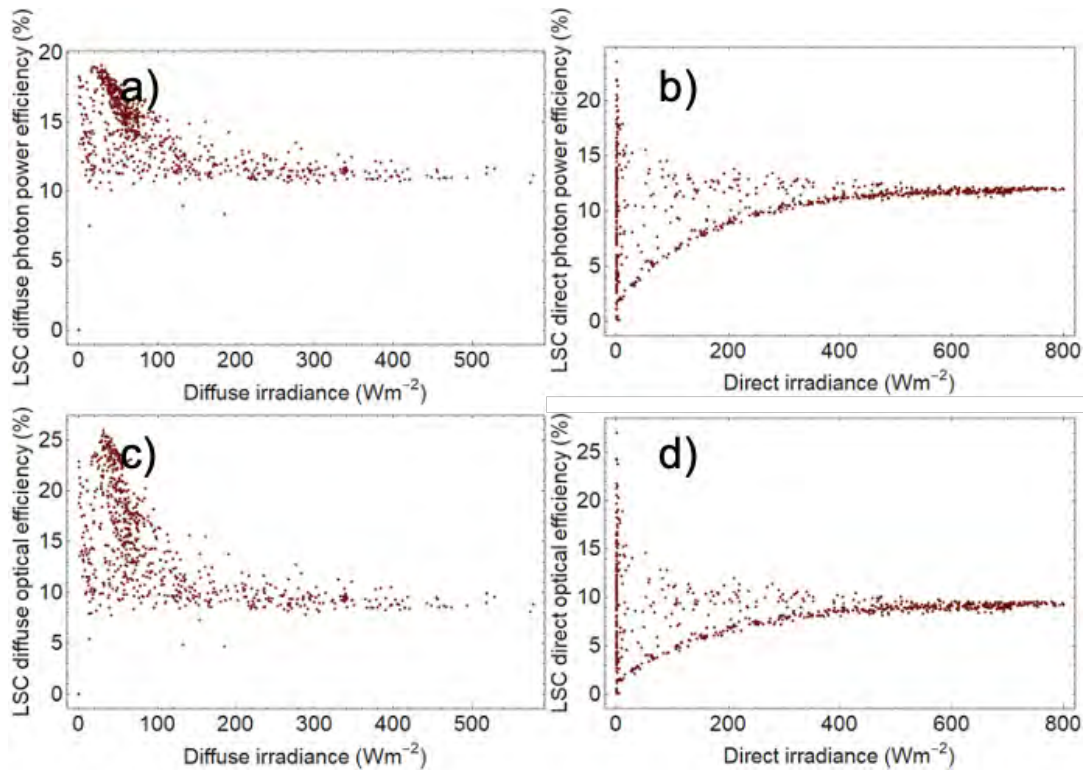
FIGURE 4.7: Lumogen 305 LSC - plots of **a** diffuse and **b** direct pho-
ton power efficiency vs spectral irradiance, and **c** diffuse and **d** direct
optical efficiency vs spectral irradiance.

The optical efficiency is calculated as $\eta_{Opt} = \frac{\text{Photons emitted by the LSC towards the Si cells}}{\text{Photons incident on the LSC}}$.
The optical efficiencies of each LSC are shown in sub-Figures **c** and **d** of Figures 4.5,
4.6, and 4.7 for diffuse and direct irradiance, respectively. These efficiencies follow
approximately the same relationships to irradiance as the photon power efficiencies,
but we see much higher values for efficiency here. Interestingly, the optical efficiency
of the Tc/PbS LSC is far higher than the Lumogen 305 LSC, often reaching in excess
of 25% and a maximum of over 70% efficiency.

The 200% PLQE Tc/PbS LSC has a range of both direct and diffuse efficiencies that
is higher than the Lumogen 305 LSC. The reason for this may be as simple as having
a more optimally positioned bandgap, but could also lie in a side benefit of hav-
ing such a large Stokes shift: We have calculated the optimal concentration of each
luminophore to maximise absorption while minimising reabsorption. The concen-
trations we have used for our simulations are 0.1 M for $Yb^{3+} : CsPb(Cl_{1-x}Br_x)_3$,
0.01 M for Tc/PbS, and 0.000001 M for Lumogen 305. The two luminophores with
large Stokes shift have almost no reabsorption, and so their concentration in the
LSC can be increased far higher when compared to Lumogen 305, with $Yb^{3+} :
CsPb(Cl_{1-x}Br_x)_3$ the highest due to having a lower molar absorption coefficient. Due
to the overlap in emission and absorption spectra (see Figure 3.5) of Lumogen 305
there is a peak in PLQE at a specific concentration, below which absorption rates are
low, and above which reabsorption rates are too high, each leading to a reduction in
efficiency.

Sources suggest tinted windows should transmit a minimum of 40% of visible pho-
tons to be practical as a window [44]. All three LSCs we have modelled here have
optical efficiencies of below 60% overall. The absorption of $Yb^{3+} : CsPb(Cl_{1-x}Br_x)_3$

begins at 400 nm, so doesn't interfere with the visible spectrum much at all. Tc absorption begins at around 550 nm, so leaves yellow/orange/red photons undisturbed, while approximately 25%-30% of the rest of the visible spectrum is absorbed. Lumogen 305 absorption causes it to look red. In our measurements it absorbs approximately 10% of all other coloured photons in the spectrum.

4.3   Efficiency and Angle of incidence

This section looks at the relationship between LSC photon power efficiency and incident angle. In these simulations the LSC is laid horizontally so the angle of incidence is simply the altitude of the Sun above the horizon, measured in single degree steps.

Figures 4.8 and 4.9 show the diffuse LSC photon power efficiencies of the Tc/PbS and Lumogen 305-based LSCs compared to the altitude of the Sun, with the colour of each point defined by the irradiance.

The diffuse measurements appear to be fairly constant at all altitudes. This is understandable as diffuse light in our model is spread equally across all angles in the sky. This removes the angle dependence of these measurements.

Higher irradiances seem to cause consistently lower efficiencies in the LSC. This will be discussed further in Section 4.4.
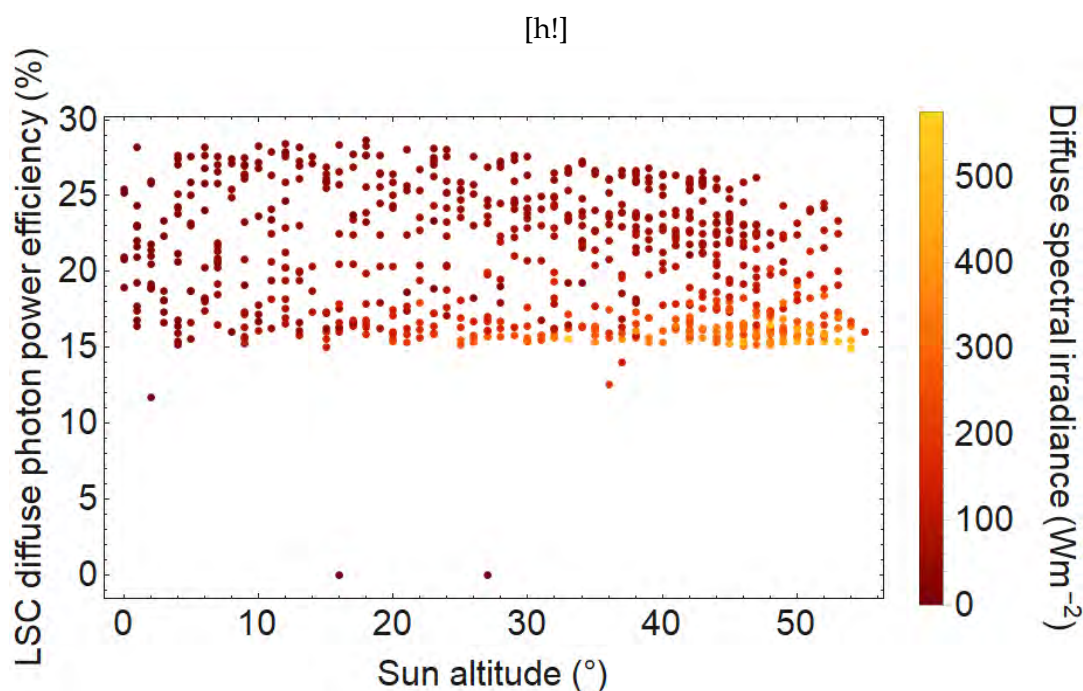
[h!]

FIGURE 4.8: PLQE = 200%, Tc/PbS LSC - plot of diffuse photon power efficiency vs angle of incidence. The points are coloured depending on the total direct spectral irradiance.
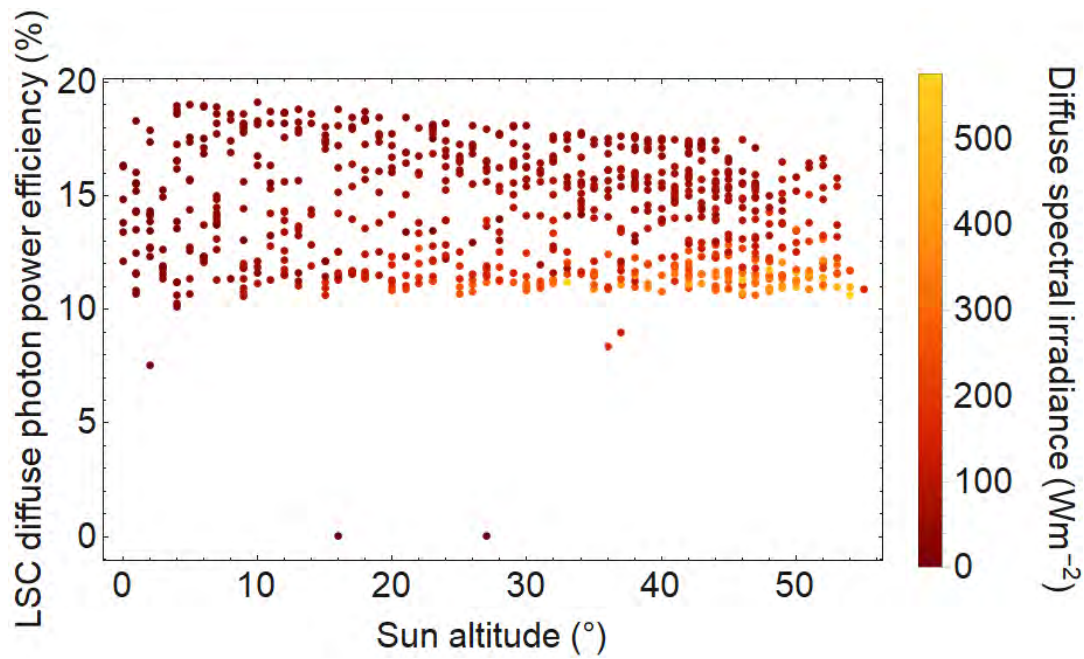
[h!]

FIGURE 4.9: Lumogen 305 LSC - plot of diffuse photon power efficiency vs angle of incidence. The points are coloured depending on the total direct spectral irradiance.

In our model we assume that diffuse light is spread equally across all angles in the sky. In real life the diffuse LSC efficiency would have a slight angle dependence, as the sky near to the Sun would have a higher irradiance than sky far from the Sun, causing a larger portion of the irradiance to be either refracted or not at the air-film interface.

The direct LSC efficiencies behave as expected as incident angle is varied. These measurements obey Fresnel's laws, with the transmission rate as the inverse of the plot shown in Figure 2.3.
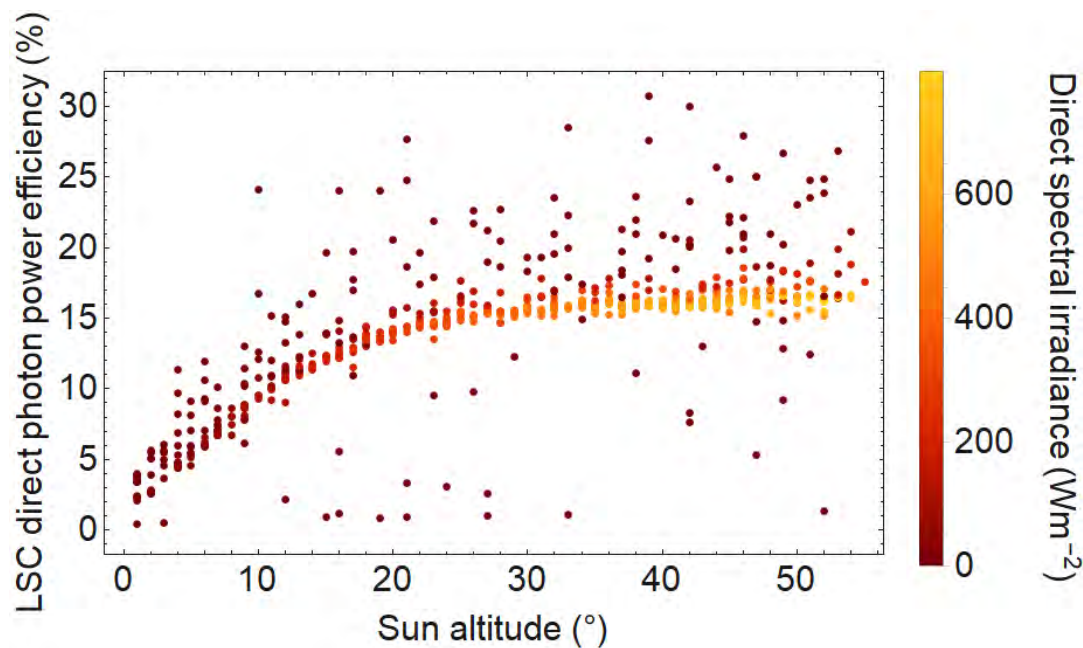
FIGURE 4.10: PLQE = 200%, Tc/PbS LSC - plot of direct photon power efficiency vs angle of incidence. The points are coloured depending on the total direct spectral irradiance.
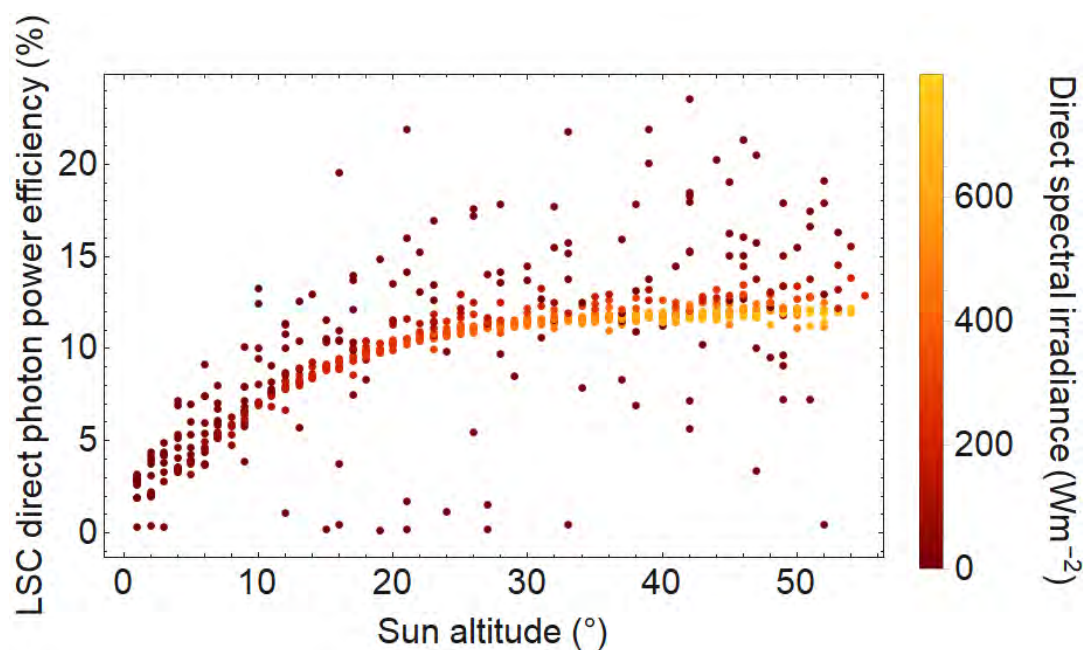

FIGURE 4.11: Lumogen 305 LSC - plot of direct photon power efficiency vs angle of incidence. The points are coloured depending on the total direct spectral irradiance.

The plots for the $Yb^{3+} : CsPb(Cl_{1-x}Br_x)_3$-based LSC are shown in Figures A.1 and A.2 in the appendix. They show a similar behaviour, but with such low LSC efficiencies it is much less apparent than for Tc/PbS and Lumogen 305.

4.4 Weather Effects on LSCs

To study the effects of weather, I have chosen two exemplary days in the month of March to compare the LSC's performance with different spectral behaviours. This will allow us to more precisely understand when and why the LSC may perform better or worse. We will look at a bright and clear day (high direct:diffuse irradiance ratio) and a cloudy day (high diffuse:direct irradiance ratio).

Figures 4.12, 4.13, and 4.14 show comparisons of LSC efficiency and irradiance over a clear day on March 16th, and an overcast day on March 30th.
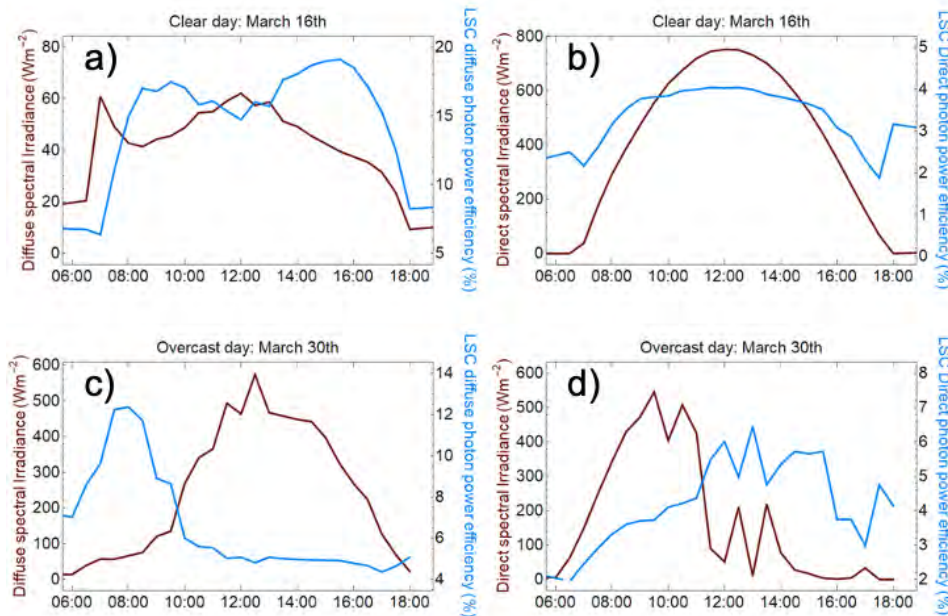

FIGURE 4.12: PLQE = 200%, $Yb^{3+} : CsPb(Cl_{1-x}Br_x)_3$ LSC - plots of LSC photon power efficiency vs irradiance on clear and overcast days for diffuse (**a**, **c**) and direct (**b**, **d**) spectra.

Photon power efficiency is expected to be lower at dawn and dusk than at midday as the solar spectrum here is very red and therefore has a very low APE, leading to little absorption in the luminophores. We observe this but also see some other very interesting behaviours in these images.

On some occasions, LSC photon power efficiency appears to mirror changes in solar irradiance. For example, on the overcast day shown in sub-Figures **c** and **d** of Figures 4.12, 4.13, and 4.14 we see an overall anti-correlation between irradiance and efficiency for both diffuse and direct measurements. In sub-Figure **c** of all LSCs diffuse irradiance is low in the morning while LSC diffuse photon power efficiency is high. This then reverses at 10:00 when diffuse irradiance becomes very high and efficiency becomes very low. Direct irradiance in sub-Figure **d** is high in the morning while efficiency is also increasing, however direct irradiance drops to very low levels at around 11:00 while efficiency increases even further. This pattern is also observed for each of the LSC simulations on a clear day when under diffuse irradiance, but not when under direct irradiance, as shown in sub-Figures **a** and **b**, respectively. For the LSCs under direct irradiance on the aforementioned clear day, the direct photon

power efficiency follows the increase and decrease in irradiance. These results indicate a similarity between diffuse behaviour in all weathers and direct behaviour on an overcast day.
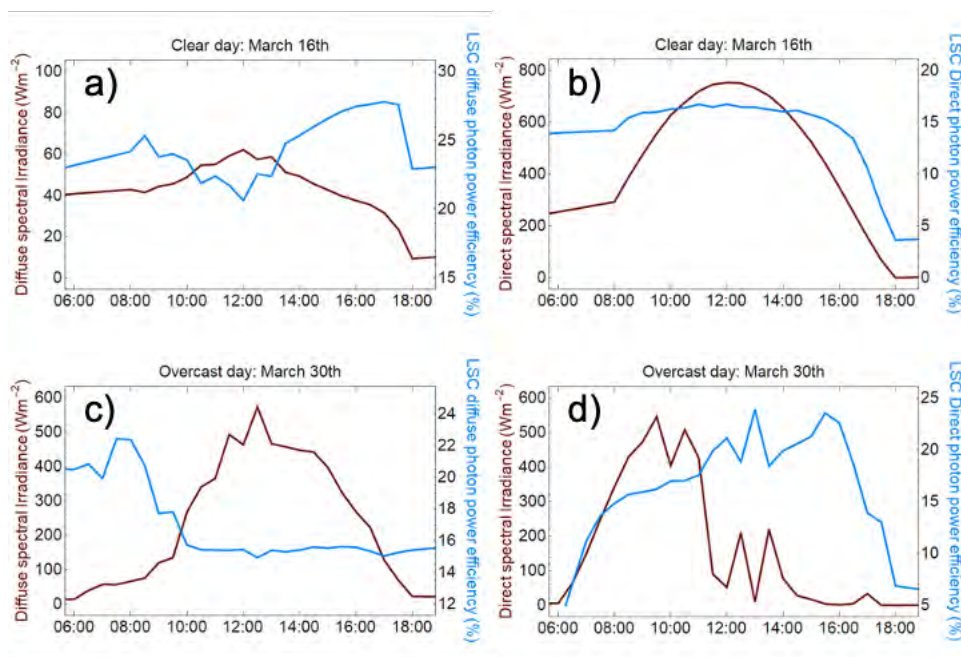

FIGURE 4.13: PLQE = 200%, Tc/PbS LSC - plots of LSC photon power efficiency vs irradiance on clear and overcast days for diffuse (**a**, **c**) and direct (**b**, **d**) spectra.

This is a behaviour also noticed by Debije et. al. in their measurements of an LSC prototype under solar irradiance [7]. An explanation of the LSC's behaviour under direct irradiation comes when considering that direct irradiance drops during the daytime when cloud coverage blocks the Sun's path to the LSC, which is prevalent in the afternoon of the overcast day. As discussed in Section 4.1, clouds reflect bluer and therefore higher APE spectra than in uninterrupted direct light, leading to a higher amount of absorption in the high-bandgap luminophores used in the LSCs while lowering overall spectral irradiance. This explains why on a clear day we see a positive relationship between direct irradiance and direct photon power efficiency while on a cloudy day we have a negative relationship.
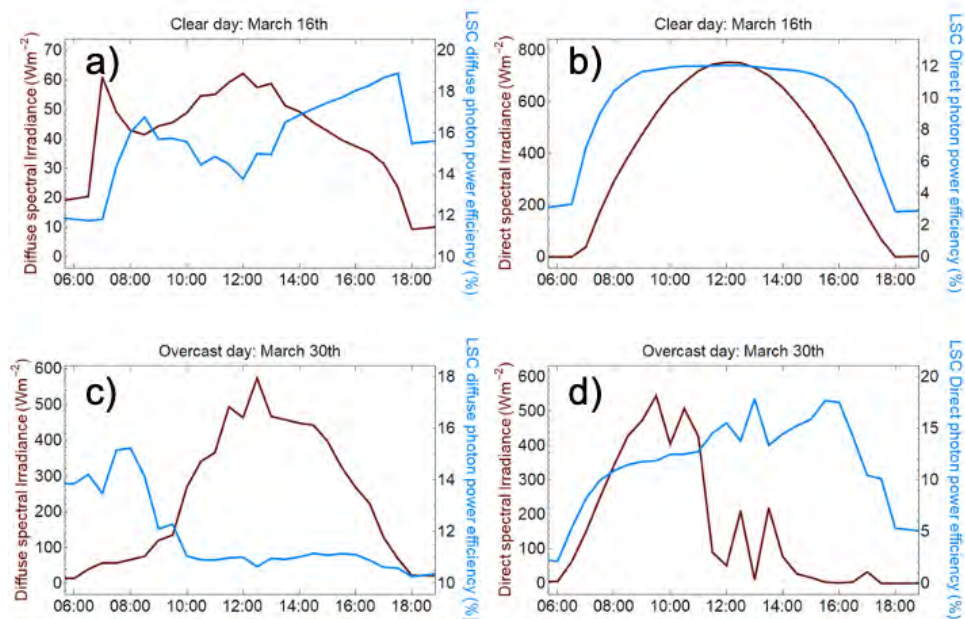
FIGURE 4.14: Lumogen 305 LSC - plots of LSC photon power efficiency vs irradiance on clear and overcast days for diffuse (**a**, **c**) and direct (**b**, **d**) spectra.

This understanding of direct efficiency variations extends to diffuse light, which is irradiance that has been scattered in the atmosphere and therefore has typically higher APEs, also shown in Section 4.1. Figures 4.15 **a** and **b** show how the diffuse photon power efficiency of the Lumogen 305-based LSC follows the changes in diffuse APE closely during the clear and overcast days, respectively.
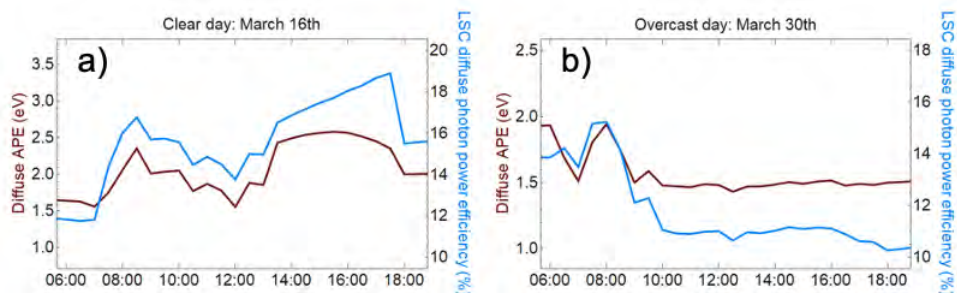

FIGURE 4.15: Lumogen 305 LSC - plots of LSC photon power efficiency vs APE on **a** clear and **b** overcast days for diffuse spectra.

The fact that diffuse irradiance increases while APE stays level, and therefore the diffuse photon power efficiency stays approximately level, is due to the counterintuitive point that a truly cloudy day would have very low irradiance and a high APE, while a thinner dispersion of cloud across the sky would be brighter (higher irradiance) but less absorbing of low energy photons, hence having a lower (or in the case of Figure 4.15 **b**, flat) APE.

4.5 LSC Output Spectra and Si Efficiency

An example of the spectra output by the LSC under direct irradiance onto all four sides where the Si cells reside is shown in Figure 4.16.
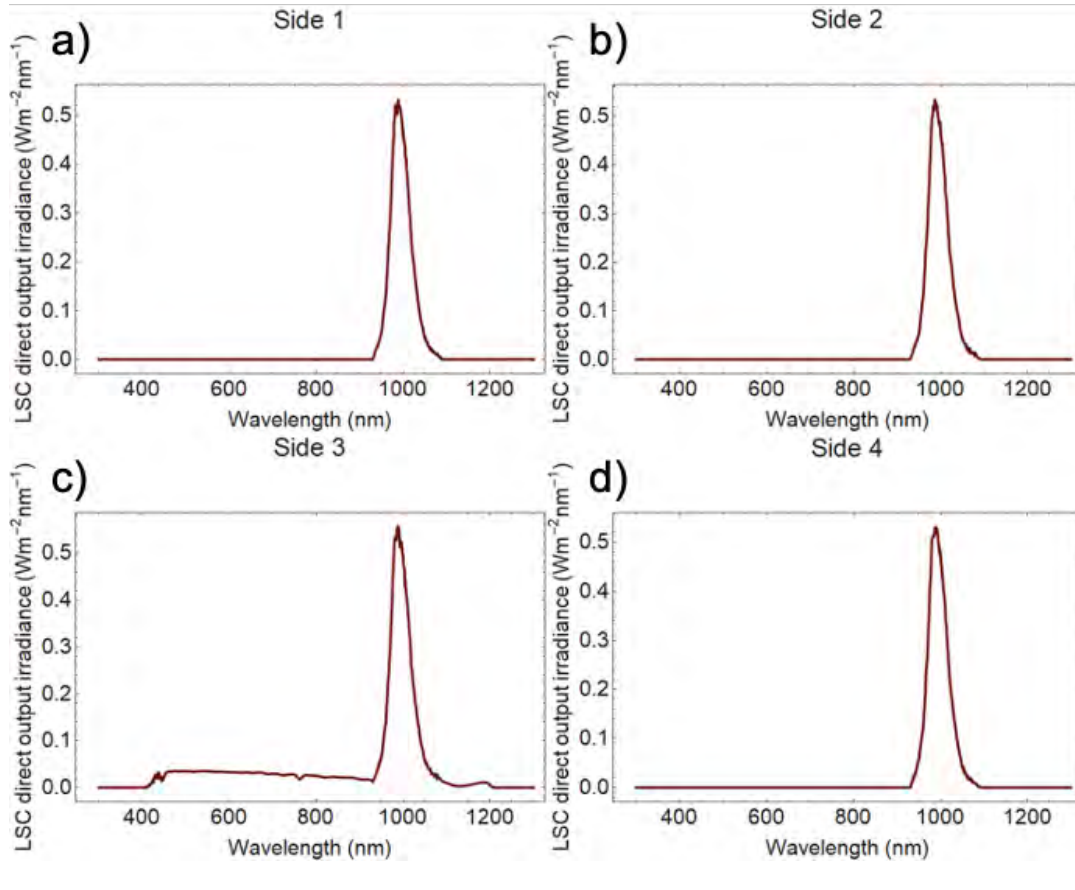

FIGURE 4.16: PLQE = 200%, Yb^{3+} : $CsPb(Cl_{1-x}Br_x)_3$ LSC - **a)**, **b, c)**, and **d)** show examples of spectral emission under direct irradiance from each of the four sides of the LSC, directed on to each Si cell. Data from 09:00 on March 16th, 2018.

The side numbers correspond to those shown in Figure 3.6, with side 3 in the receiving direction of incident spectral photons. We see the outcome of this in Figure 4.16 **c)** where the emission spectrum is much broader than for the other three sides. This occurs as, particularly at low solar altitudes, a portion of the incident spectrum that is transmitted into the LSC is aimed at the Si cell on the side directly. Therefore, some photons that would normally not be absorbed by the luminophore still reach the Si cell. Shown in Table 4.1, this can either benefit or downgrade the electrical power efficiency of the Si cell positioned on side 3, depending on the correlation between emission of the luminophore and absorption of the Si. Table 4.1 shows the efficiencies recorded in each of the Si cells for all three LSCs, measured at the same point in time as Figure 4.16: 09:00 on March 16th.

The performance of the Si cells relies on the emission of the luminophore used. We can see in Figure 4.16 that the Yb^{3+} emission is almost perfect for the Si bandgap of 1107 nm, which is shown in the very high efficiencies recorded in Table 4.1. This direct spectral transmission therefore affects the efficiency of cell 3 negatively in the Yb^{3+} : $CsPb(Cl_{1-x}Br_x)_3$-based LSC. The emission spectra of PbS, shown in Figure

Luminophore	Cell 1	Cell 2	Cell3	Cell 4
Yb	42.66%	42.68%	39.43%	42.73%
PbS	0.85%	0.85%	2.51%	0.87%
Lumo	30.40%	30.43%	30.69%	30.47%

TABLE 4.1: Silicon solar cell electrical power efficiencies on each of the four sides of each LSC. Data recorded at 09:00 on March 16th, 2018.

A.5 of the appendix, is almost entirely below the Si bandgap leading to very low efficiencies, while the Lumogen 305 (Figure A.6 of the appendix) emission is centred approximately 1.5x above the Si bandgap and hence we achieve reasonable Si power efficiencies, although notably lower than the Yb^{3+}.

4.6 Comparing kWh

In this section we compare the electrical output of our three LSC/Si cells with the electrical output of a Si solar cell only, over the month of March, 2018. The Si cell used is the same record solar cell that is modelled for each of the sides of the LSC [13].

In Table 4.2, the kWh for each LSC simulation is totalled for the spectral irradiance, the LSC photon output power on to each side, and for the full LSC+Si system's electrical output power, as well as the electrical power for the lone Si cell.

PV cell	Total spectral kWh m^{-2}	LSC kWh m^{-2}	Full system kWh m^{-2}
Yb-LSC	153.67	7.45	2.94
PbS-LSC	149.33	24.50	0.30
Lumo-LSC	155.00	18.35	5.60
Si cell	155.16	-	40.96

TABLE 4.2: Total kWh achieved in the full month of March, 2018 (i.e. kWh m^{-2} month^{-1} for each luminophore-based LSC, as compared to a Si cell on its own. Total spectral kWh m^{-2} is the total spectral energy over the full month, LSC kWh m^{-2} is the total energy output of the LSC out through its four thin sides, and Full system kWh m^{-2} is the electrical energy produced by either the full LSC/Si system, or the Si cell on its own.

We note that in Table 4.2 each simulation has a small variation in total spectral kWh m^{-2} month^{-1}, but this is a systematic error in running the code. The simulation was run for a full year with many thousands of data files that were sent to a supercomputer to run, and so a few files in every several thousand may have been skipped by the system.

The results in Table 4.2 tell us a lot about the capabilities of the LSCs we have modelled. The absorption of the $CsPb(Cl_{1-x}Br_x)_3$ is very high, leading to very low LSC efficiencies that affect the system massively despite very high Si efficiencies (around 35% on average). The Tc/PbS system has excellent absorption but the emission is too low in energy for the Si, causing electrical efficiencies to be very low. The Lumogen 305 system is a good middle ground in both areas, with good absorption and

very reasonable Si efficiencies. None of the LSCs can beat the Si cell on its own, even when comparing the photon output power of each LSC with the Si cell-only's electrical power out, which is understandable when considering that the Si cell is designed to absorb everything it can, while the LSCs are designed to be partially transparent for use as solar windows.

Lumogen 305 achieves the best results in this simulation, however this was run for an LSC of dimensions 10cm x 10cm x $\frac{1}{3}$cm. The issue of losses through reabsorption in dyes is far more pronounced for larger LSCs, as the likelihood of reabsorption increases, so we would expect to see this drop in efficiency when applied to real window dimensions.

A back-of-the-envelope calculation we can do is to estimate the earnings per unit area of each LSC based on their energy output. The average cost of electricity in the UK is around 14.37p per kWh [45].

PV cell	Total LSC/Si kWh m^{-2}	Earnings £ m^{-2}
Yb-LSC	2.94	£0.42 m^{-2}
PbS-LSC	0.30	£0.04 m^{-2}
Lumo-LSC	5.60	£0.80 m^{-2}
Si cell	40.96	£5.88 m^{-2}

TABLE 4.3: Total kWh achieved in the full month of March, 2018, along with the savings in £ per metre squared of each luminophore-based LSC as compared with a Si cell on its own, calcualted using the average cost of electricity in the UK of 14.37p [45]

In these simulations over a single month, the Si cell on its own has by far the biggest electrical payback, with a total monthly electricity production earning of £5.88 m^{-2}. For a solar panel setup of 5m x 2m this could earn the owner £59 per month in electricity. The Yb^{3+} : CsPb(Cl$_{1-x}$Br$_x$)$_3$-based LSC achieves the highest of the PM luminophores, with around $\frac{1}{14}$ of the earnings of the Si, i.e. 10 m^2 of surface area could earn £4.20 through electricity production per month.

Chapter 5

Conclusions and Outlook

5.1   Conclusions

The aim of this collaborative project was to create a model of a luminescent solar concentrator (LSC) with silicon (Si) cells attached to each side, and to simulate its performance under realistic spectral conditions.

In this report, we have modelled three LSCs in a semi-transparent setup, each with Si solar cells attached to all four sides. The LSCs are based on three different luminophores doped in a PLMA host matrix. The three luminophores we have modelled are a tried-and-tested Lumogen 305 dye with transparency in the red part of the visible spectrum, and two photon multiplying (PM) luminophores. Yb^{3+}-doped $CsPb(Cl_{1-x}Br_x)_3$ is a nanocrystal (NC) that exhibits quantum cutting (QC), a form of PM that occurs through a Yb^{3+}-induced defect state. Another PM luminophore we modelled is the organic material tetracene (Tc) coupled with PbS QDs. Tc can split a single high energy singlet state into two low energy triplet states, a process called singlet fission (SF). These triplets are then transferred to the PbS QDs for efficient emission. Both PM luminophores are modelled at a fixed PLQE of 200%. Using spectral data from The National Renewable Energy Laboratory (NREL) in Denver, Colorado, we have simulated the performance of these LSCs over the full month of March, 2018.

The Lumogen 305-based LSC achieved the highest electrical efficiency of the LSCs tested despite being at a comparatively low concentration of 0.000001 M, however Lumogen 305 has a very small Stokes shift that leads to a larger number of photons that undergo reabsorption, constituting a loss in efficiency for LSCs of increasing size, making it not recommendable for real-world window applications.

The QC Yb^{3+} : $CsPb(Cl_{1-x}Br_x)_3$-based LSC showed low photon power conversion efficiencies of around 5% due to a very high-energy absorption spectra beginning around 3eV in the $CsPb(Cl_{1-x}Br_x)_3$ perovskite leading to very little of the solar spectra being absorbed. There are, however, benefits to this as the visible spectrum is almost fully transmitted, making it an excellent luminophore for a clear solar window. The Yb^{3+} emission matches the Si cell absorption very well, so adjustment of the absorption spectra to lower energies could have large effects in increasing LSC efficiency.

The SF Tc/PbS LSC has promising absorption in the 400nm - 550nm region, giving it a high photon power efficiency, however huge losses occur in photon absorption in the Si cells due to a very low-energy PbS emission, with only a few percent of all photons emitted lying above the Si bandgap. The PbS emission can be tuned

through quantum confinement, allowing a realistic shift towards higher energies, so long as they are below half the Tc bandgap for SF to occur.

The SF and QC luminophores have been held at a constant PLQE of 200% for all of these simulations. This represents exactly two photons emitted for each photon absorbed by the luminophores. For the QC Yb^{3+} : $CsPb(Cl_{1-x}Br_x)_3$, this is a realistically achievable value in the future, with current records at 190% PLQE, however saturation when under modest fluence is this luminophore's major pitfall [46][26]. The Tc/PbS combination has been synthesised to achieve maximum efficiencies (100%) in all areas apart from photoluminescence (PL), so far. However, it is expected to be possible to independently improve PL without compromising the other steps, creating optimism in reaching near-200% PLQEs here, too [30].

Windows should transmit above 40% of incident visible photons to be transparent enough for buildings requiring reasonable amounts of natural light [44]. All three LSCs we have modelled have optical efficiencies in the visible range of less than 60% and are evidently all acceptable in a window format. As the Yb^{3+} : $CsPb(Cl_{1-x}Br_x)_3$ absorption begins at energies at the very violet end of the visible spectrum, it gives allowance for a shift towards lower absorption energies and therefore higher optical and power efficiencies. For QC to happen, it must be situated at least twice the bandgap of the Yb^{3+} ions, implying a potential shift towards 2.5eV - in the range of cyan and blue light.

The results in this thesis show that LSCs respond better to diffuse irradiance than direct, with higher efficiencies occuring in very cloudy weather. LSCs are evidently most beneficial in cloudy locations, with efficiencies closely following the average photon energy (APE) of the solar spectrum, which in turn increases as reflection from clouds increases. The ability to concentrate diffuse irradiation This would suit such as cities and typically cloudy countries in Northern Europe and Asia.

The results in this thesis show that LSCs respond better to diffuse irradiance than direct, with higher efficiencies occurring in very cloudy weather; LSC efficiencies closely follow the average photon energy (APE) of the solar spectrum, which in turn increases as reflection from clouds increases. The photon power and optical efficiencies under diffuse irradiance rarely drop below certain values for each LSC, while direct efficiency climbs and falls with direct irradiance. The LSC would evidently suit locations such as cities and typically cloudy countries in Northern Europe and Asia.

The model created provides a basis that will allow for easy expansion to model LSCs of different configurations and environmental conditions in the future.

5.2 Outlook

The work described in this thesis is ongoing by collaborators in Cambridge University, UK and AMOLF, NL, with several possible steps to improve further results and comparisons for photon-multiplier-based LSCs.

The results of this thesis show that the absorption spectra of the $CsPb(Cl_{1-x}Br_x)_3$ perovskite is too high. Shifting absorption further into the visible spectrum would allow for a far more efficient LSC. The emission spectrum of the PbS quantum dots is too low in energy, causing electrical power efficiency to be extremely low. PbS

emission should be altered to match the Si absorption, which is possible by adjusting the size of the QD. However, this is where experimental problems arise.

An unfortunate error in the Colorado spectral code lead to all months except March having an incorrect solar zenith angle - this is repairable. We also now have spectral data from Amsterdam that can be applied to the LSCs for a comparison in performance between two very different climates. This will shed light on the weather- and therefore location-related performance of the LSCs.

The LSC can be designed in different shapes, dimensions, and with diffusive back-reflectors, and even multiple luminophores for varying the amount of absorption achieved by the device. Future work can look into optimising these factors to create the most efficient window/wall photovoltaic LSC possible.

We have only modelled the LSC in a horizontal format. It would be ideal to rotate it to be in a vertical position for use in a window, or another angle such as $40°$, South-facing for ideal absorption.

Lastly, an investigation into the levelised cost of energy (LCOE) would conclude how competitive, and how financially feasible the LSCs discussed in this thesis can be.

Appendix A

Further plots
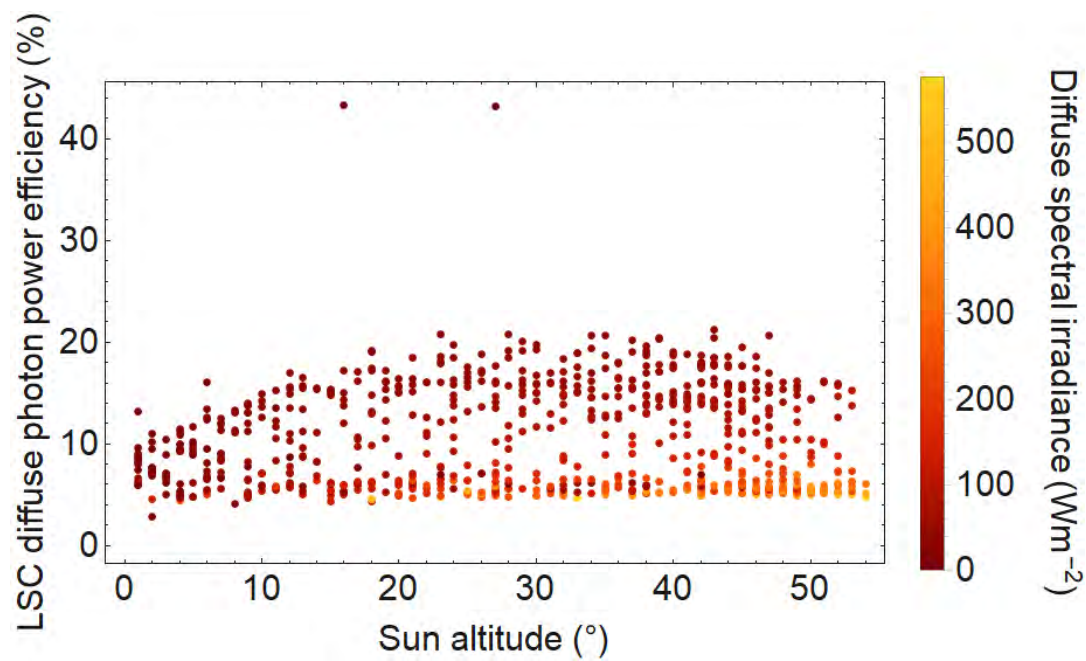
A.1 Efficiency and angle of incidence

FIGURE A.1: PLQE = 200%, Yb^{3+} : $CsPb(Cl_{1-x}Br_x)_3$ LSC - plot of diffuse photon power efficiency vs angle of incidence.
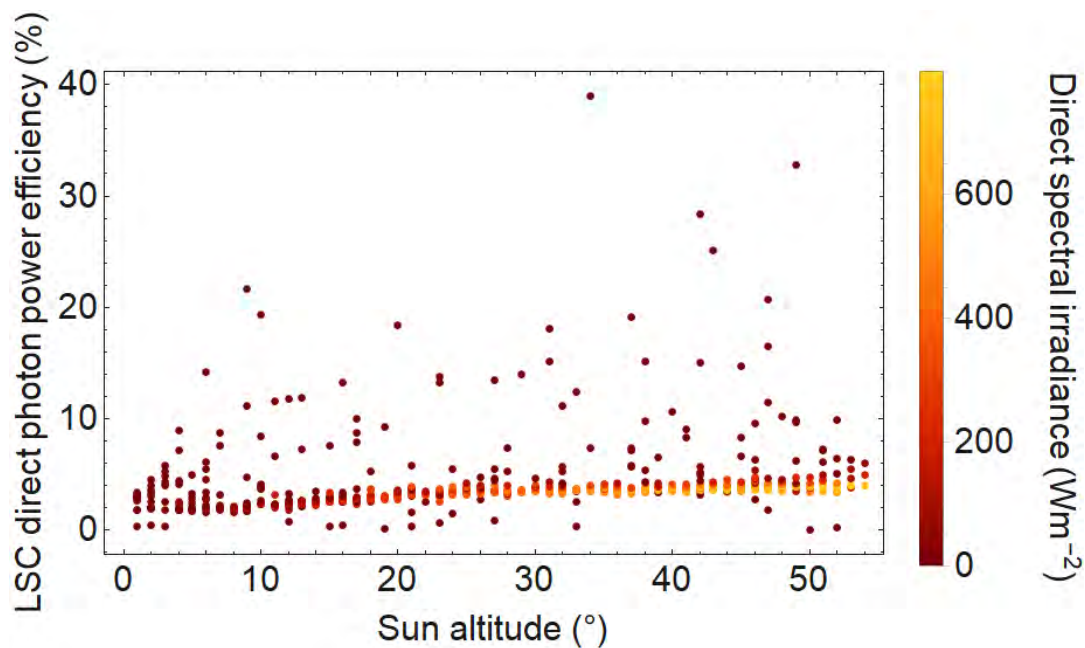
FIGURE A.2: PLQE = 200%, Yb^{3+} : $CsPb(Cl_{1-x}Br_x)_3$ LSC - plot of direct photon power efficiency vs angle of incidence.
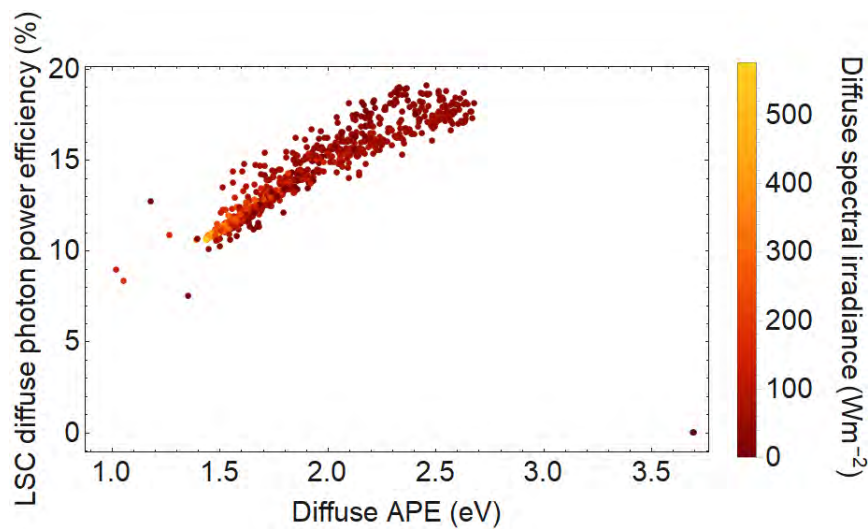
A.2　Average photon energy

FIGURE A.3: Lumogen 305 LSC photon power efficiency related to the spectral APE for diffuse irradiation. The points are coloured depending on the total diffuse spectral irradiance.
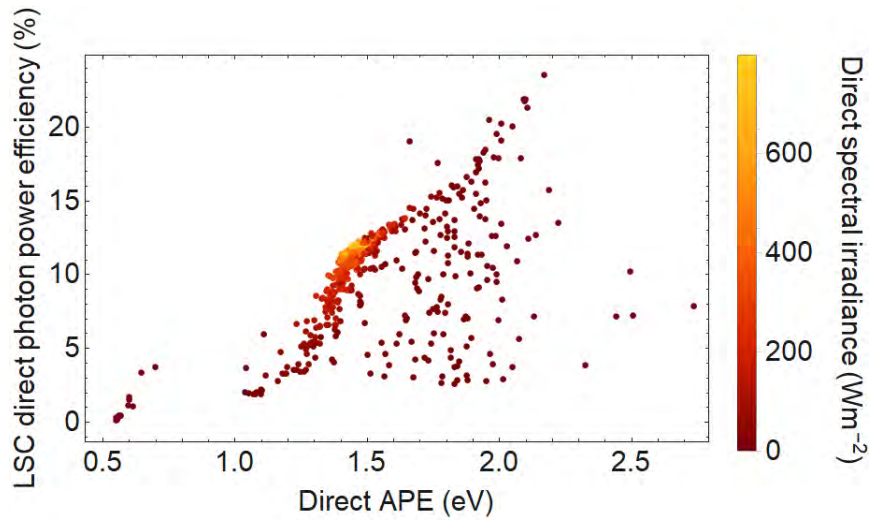
FIGURE A.4: Lumogen 305 LSC photon power efficiency related to the spectral APE for direct irradiation. The points are coloured depending on the total direct spectral irradiance.
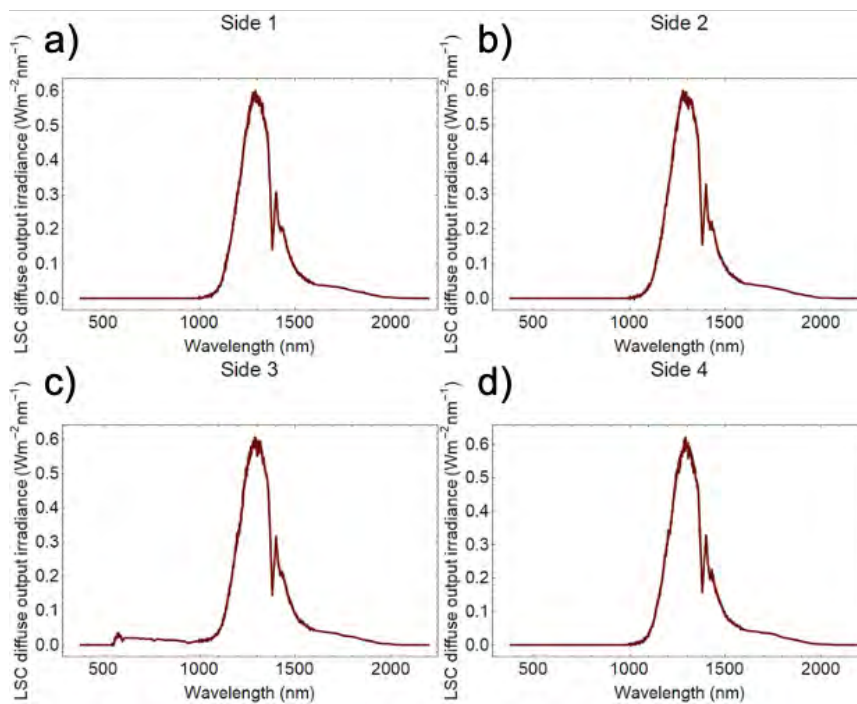
A.3 LSC output spectra

FIGURE A.5: PLQE=200%, Tc/PbS LSC - **a)**, **b**, **c)**, and **d)** show examples of spectral emission under direct irradiance from each of the four sides of the LSC, directed on to each Si cell.
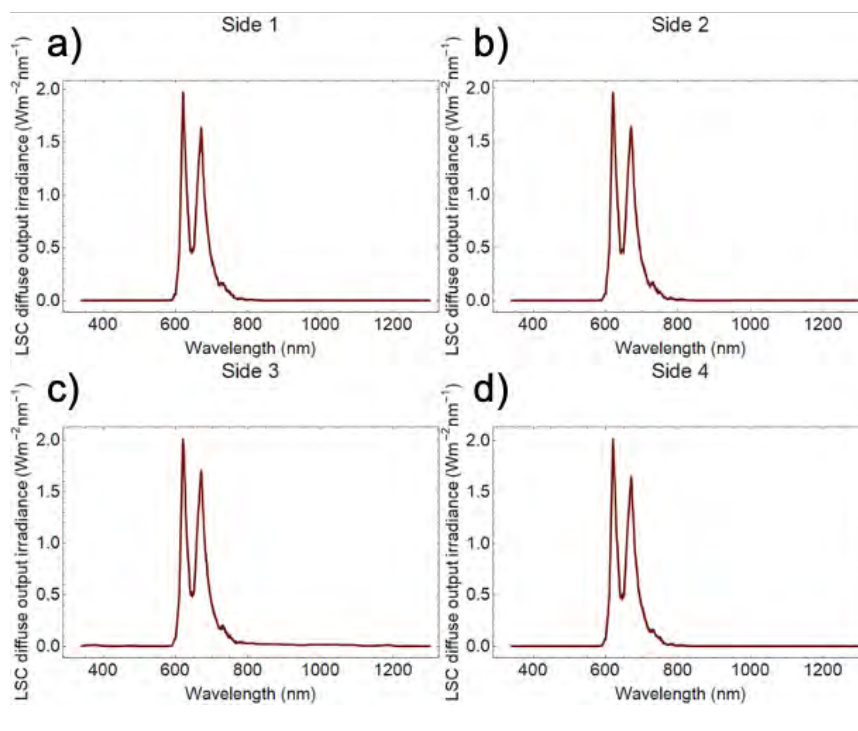
FIGURE A.6: Lumogen 305 LSC - **a)**, **b**, **c)**, and **d)** show examples of spectral emission under direct irradiance from each of the four sides of the LSC, directed on to each Si cell.

Bibliography

[1] *Cost of Renewable Technologies: Solar PV*. URL: https://ourworldindata.org/renewable-energy#cost-of-renewable-technologies. (accessed: 13/07/2020).

[2] L. H. Slooff et al. "A luminescent solar concentrator with 7.1% power conversion efficiency". In: *physica status solidi (RRL) – Rapid Research Letters* 2.6 (2008), pp. 257–259. DOI: 10.1002/pssr.200802186. eprint: https://onlinelibrary.wiley.com/doi/pdf/10.1002/pssr.200802186. URL: https://onlinelibrary.wiley.com/doi/abs/10.1002/pssr.200802186.

[3] CurrentResults. URL: https://www.currentresults.com/Weather-Extremes/Europe/cloudiest-cities.php. (accessed: 22/08/2020).

[4] J. Roncali and F. Garnier. "Photon-transport properties of luminescent solar concentrators: analysis and optimization". In: *Appl. Opt.* 23.16 (1984), pp. 2809–2817. DOI: 10.1364/AO.23.002809. URL: http://ao.osa.org/abstract.cfm?URI=ao-23-16-2809.

[5] Michael G. Debije and Vikram A. Rajkumar. "Direct versus indirect illumination of a prototype luminescent solar concentrator". In: *Solar Energy* 122 (2015), pp. 334 –340. ISSN: 0038-092X. DOI: https://doi.org/10.1016/j.solener.2015.08.036. URL: http://www.sciencedirect.com/science/article/pii/S0038092X15004867.

[6] UbiQD. URL: https://twitter.com/UbiQD/status/951823775816806400/photo/3. (accessed: 15/07/2020).

[7] Michael G. Debije and Paul P. C. Verbunt. "Thirty Years of Luminescent Solar Concentrator Research: Solar Energy for the Built Environment". In: *Advanced Energy Materials* 2.1 (2012), pp. 12–35. DOI: 10.1002/aenm.201100554. eprint: https://onlinelibrary.wiley.com/doi/pdf/10.1002/aenm.201100554. URL: https://onlinelibrary.wiley.com/doi/abs/10.1002/aenm.201100554.

[8] Yilin Li et al. "Review on the Role of Polymers in Luminescent Solar Concentrators". In: *Journal of Polymer Science Part A: Polymer Chemistry* 57.3 (2019), pp. 201–215. DOI: 10.1002/pola.29192. eprint: https://onlinelibrary.wiley.com/doi/pdf/10.1002/pola.29192. URL: https://onlinelibrary.wiley.com/doi/abs/10.1002/pola.29192.

[9] Ryan Connell et al. "CdSe/CdS–poly(cyclohexylethylene) thin film luminescent solar concentrators". In: *APL Materials* 7.10 (2019), p. 101123. DOI: 10.1063/1.5121441. URL: https://doi.org/10.1063/1.5121441.

[10] Francesco Meinardi et al. "Doped Halide Perovskite Nanocrystals for Reabsorption-Free Luminescent Solar Concentrators". In: *ACS Energy Letters* 2.10 (2017), pp. 2368–2377. DOI: 10.1021/acsenergylett.7b00701.

[11] Zachar Krumer et al. "Tackling self-absorption in luminescent solar concentrators with type-II colloidal quantum dots". In: *Solar Energy Materials and Solar Cells* 111 (2013), pp. 57 –65. ISSN: 0927-0248. DOI: https://doi.org/10.1016/j.solmat.2012.12.028. URL: http://www.sciencedirect.com/science/article/pii/S0927024812005582.

[12] *Recombination Calculator*. URL: https://www2.pvlighthouse.com.au/calculators/Recombination%20calculator/Recombination%20calculator.aspx. (accessed: 08/06/2020).

[13] Kunta Yoshikawa et al. "Exceeding conversion efficiency of 26interdigitated back contact solar cell with thin film Si technology". In: *Solar Energy Materials and Solar Cells* 173 (2017). Proceedings of the 7th international conference on Crystalline Silicon Photovoltaics, pp. 37 –42. ISSN: 0927-0248. DOI: https://doi.org/10.1016/j.solmat.2017.06.024. URL: http://www.sciencedirect.com/science/article/pii/S092702481730332X.

[14] A. Goetzberger. "Fluorescent solar energy collectors: Operating conditions with diffuse light". In: *Applied physics* 16.4 (1978), pp. 399–404. DOI: 10.1007/BF00885865. URL: https://doi.org/10.1007/BF00885865.

[15] Renata Reisfeld and Yehoshua Kalisky. "Improved planar solar converter based on uranyl neodymium and holmium glasses". In: *Nature* 283.5744 (1980), pp. 281–282. DOI: 10.1038/283281a0. URL: https://doi.org/10.1038/283281a0.

[16] Renata Reisfeld and Samuel Neuman. *Planar solar energy converter and concentrator based on uranyl-doped glass*. 1978. DOI: 10.1038/274144a0.

[17] J. A. Levitt and W. H. Weber. "Materials for luminescent greenhouse solar collectors". In: *Appl. Opt.* 16.10 (Oct. 1977), pp. 2684–2689. DOI: 10.1364/AO.16.002684. URL: http://ao.osa.org/abstract.cfm?URI=ao-16-10-2684.

[18] Liam R. Bradshaw et al. "Nanocrystals for Luminescent Solar Concentrators". In: *Nano Letters* 15.2 (2015). PMID: 25585039, pp. 1315–1323. DOI: 10.1021/nl504510t.

[19] Xiao Luo et al. "Quantum-Cutting Luminescent Solar Concentrators Using Ytterbium-Doped Perovskite Nanocrystals". In: *Nano Letters* 19.1 (2019), pp. 338–341. DOI: 10.1021/acs.nanolett.8b03966. URL: https://doi.org/10.1021/acs.nanolett.8b03966.

[20] Qingsong Hu et al. "Rare Earth Ion-Doped CsPbBr3 Nanocrystals". In: *Advanced Optical Materials* 6.2 (2018), p. 1700864. DOI: 10.1002/adom.201700864. URL: https://onlinelibrary.wiley.com/doi/abs/10.1002/adom.201700864.

[21] Theodore A. Cohen et al. "Quantum-cutting Yb3+-doped perovskite nanocrystals for monolithic bilayer luminescent solar concentrators". In: *J. Mater. Chem. A* 7 (15 2019), pp. 9279–9288. DOI: 10.1039/C9TA01261C. URL: http://dx.doi.org/10.1039/C9TA01261C.

[22] Donglei Zhou et al. "Cerium and Ytterbium Codoped Halide Perovskite Quantum Dots: A Novel and Efficient Downconverter for Improving the Performance of Silicon Solar Cells". In: *Advanced Materials* 29.42 (2017), p. 1704149. DOI: 10.1002/adma.201704149. URL: https://onlinelibrary.wiley.com/doi/abs/10.1002/adma.201704149.

[23] Tyler J. Milstein et al. "Anion Exchange and the Quantum-Cutting Energy Threshold in Ytterbium-Doped CsPb(Cl1−xBrx)3 Perovskite Nanocrystals". In: *Nano Letters* 19.3 (2019). PMID: 30694072, pp. 1931–1937. DOI: 10.1021/acs.nanolett.8b05104. URL: https://doi.org/10.1021/acs.nanolett.8b05104.

[24] Tyler J. Milstein, Daniel M. Kroupa, and Daniel R. Gamelin. "Picosecond Quantum Cutting Generates Photoluminescence Quantum Yields Over 100% in Ytterbium-Doped CsPbCl3 Nanocrystals". In: *Nano Letters* 18.6 (2018). PMID: 29746137, pp. 3792–3799. DOI: 10.1021/acs.nanolett.8b01066.

[25] Wasim J. Mir et al. "Postsynthesis Doping of Mn and Yb into CsPbX3 (X = Cl, Br, or I) Perovskite Nanocrystals for Downconversion Emission". In: *Chemistry of Materials* 30.22 (2018), pp. 8170–8178. DOI: 10.1021/acs.chemmater.8b03066.

[26] Christian S. Erickson et al. "Photoluminescence Saturation in Quantum-Cutting Yb3+-Doped CsPb(Cl1–xBrx)3 Perovskite Nanocrystals: Implications for Solar Downconversion". In: *The Journal of Physical Chemistry C* 123.19 (2019), pp. 12474–12484. DOI: 10.1021/acs.jpcc.9b01296. URL: https://doi.org/10.1021/acs.jpcc.9b01296.

[27] Moritz H. Futscher, Akshay Rao, and Bruno Ehrler. "The Potential of Singlet Fission Photon Multipliers as an Alternative to Silicon-Based Tandem Solar Cells". In: *ACS Energy Letters* 3.10 (2018). PMID: 30345370, pp. 2587–2592. DOI: 10.1021/acsenergylett.8b01322. URL: https://doi.org/10.1021/acsenergylett.8b01322.

[28] Millicent B. Smith and Josef Michl. "Singlet Fission". In: *Chemical Reviews* 110.11 (2010). PMID: 21053979, pp. 6891–6936. DOI: 10.1021/cr1002613. eprint: https://doi.org/10.1021/cr1002613. URL: https://doi.org/10.1021/cr1002613.

[29] Stefan W. Tabernig et al. "Enhancing silicon solar cells with singlet fission: the case for Förster resonant energy transfer using a quantum dot intermediate". In: *Journal of Photonics for Energy* 8.2 (2018), pp. 1 –12. DOI: 10.1117/1.JPE.8.022008. URL: https://doi.org/10.1117/1.JPE.8.022008.

[30] Nathaniel J. L. K. Davis et al. "Singlet Fission and Triplet Transfer to PbS Quantum Dots in TIPS-Tetracene Carboxylic Acid Ligands". In: *The Journal of Physical Chemistry Letters* 9.6 (2018). PMID: 29506386, pp. 1454–1460. DOI: 10.1021/acs.jpclett.8b00099. URL: https://doi.org/10.1021/acs.jpclett.8b00099.

[31] Nicholas J. Thompson et al. "Energy harvesting of non-emissive triplet excitons in tetracene by emissive PbS nanocrystals". In: *Nature Materials* 13.11 (2014), pp. 1039–1043. DOI: 10.1038/nmat4097. URL: https://doi.org/10.1038/nmat4097.

[32] Afshin Andreas and Tom Stoffel. *NREL Solar Radiation Research Laboratory (SRRL): Baseline Measurement System (BMS)*. Tech. rep. Golden, Colorado (Data): NREL, 1981, pp. 5500–56488. DOI: 10.5439/1052221.

[33] Moritz H. Futscher and Bruno Ehrler. "Modeling the Performance Limitations and Prospects of Perovskite/Si Tandem Solar Cells under Realistic Operating Conditions". In: *ACS Energy Letters* 2.9 (2017). PMID: 28920081, pp. 2089–2095. DOI: 10.1021/acsenergylett.7b00596. URL: https://doi.org/10.1021/acsenergylett.7b00596.

[34] Moritz H. Futscher and Bruno Ehrler. "Efficiency Limit of Perovskite/Si Tandem Solar Cells". In: *ACS Energy Letters* 1.4 (2016), pp. 863–868. DOI: 10.1021/acsenergylett.6b00405. URL: https://doi.org/10.1021/acsenergylett.6b00405.

[35] William Shockley and Hans J. Queisser. "Detailed Balance Limit of Efficiency of p-n Junction Solar Cells". In: *Journal of Applied Physics* 32.3 (1961), pp. 510–519. DOI: 10.1063/1.1736034. URL: https://doi.org/10.1063/1.1736034.

[36] Jenny Nelson. *The Physics of Solar Cells*. PUBLISHED BY IMPERIAL COLLEGE PRESS and DISTRIBUTED BY WORLD SCIENTIFIC PUBLISHING CO., 2003. DOI: 10.1142/p276. eprint: https://www.worldscientific.com/doi/pdf/10.1142/p276. URL: https://www.worldscientific.com/doi/abs/10.1142/p276.

[37] Kunta Yoshikawa et al. "Silicon heterojunction solar cell with interdigitated back contacts for a photoconversion efficiency over 26%". In: *Nature Energy* 2.5 (2017), p. 17032. DOI: 10.1038/nenergy.2017.32. URL: https://doi.org/10.1038/nenergy.2017.32.

[38]   Konstantinos Misiakos and Dimitris Tsamakis. "Accurate measurements of
       the silicon intrinsic carrier density from 78 to 340 K". In: *Journal of Applied
       Physics* 74.5 (1993), pp. 3293–3297. DOI: 10.1063/1.354551. URL: https://
       doi.org/10.1063/1.354551.

[39]   J. Dziewior and W. Schmid. "Auger coefficients for highly doped and highly
       excited silicon". In: *Applied Physics Letters* 31.5 (1977), pp. 346–348. DOI: 10.
       1063/1.89694. URL: https://doi.org/10.1063/1.89694.

[40]   Y.P. Varshni. "Temperature dependence of the energy gap in semiconductors".
       In: *Physica* 34.1 (1967), pp. 149 –154. ISSN: 0031-8914. DOI: https://doi.org/
       10.1016/0031-8914(67)90062-6. URL: http://www.sciencedirect.com/
       science/article/pii/0031891467900626.

[41]   S. M. Sze and N. K. Kwok. *Physics of Semiconductor Devices, 3rd Edition*. John
       Wiley & Sons Inc, 2006, pp. 739–751. URL: https://www.wiley.com/en-nl/
       Physics+of+Semiconductor+Devices{\%}2C+3rd+Edition-p-9780470068304
       (visited on 07/09/2020).

[42]   Keith R. McIntosh, Malcolm D. Abbott, and Ben A. Sudbury. "Ray Tracing
       Isotextured Solar Cells". In: *Energy Procedia* 92 (2016). Proceedings of the 6th
       International Conference on Crystalline Silicon Photovoltaics (SiliconPV 2016),
       pp. 122 –129. ISSN: 1876-6102. DOI: https://doi.org/10.1016/j.egypro.
       2016.07.041. URL: http://www.sciencedirect.com/science/article/pii/
       S1876610216304684.

[43]   G. Nofuentes et al. "Is the average photon energy a unique characteristic of the
       spectral distribution of global irradiance?" In: *Solar Energy* 149 (2017), pp. 32
       –43. ISSN: 0038-092X. DOI: https://doi.org/10.1016/j.solener.2017.
       03.086. URL: http://www.sciencedirect.com/science/article/pii/
       S0038092X17302797.

[44]   Matthew R. Bergren et al. "High-Performance CuInS2 Quantum Dot Lami-
       nated Glass Luminescent Solar Concentrators for Windows". In: *ACS Energy
       Letters* 3.3 (2018), pp. 520–525. DOI: 10.1021/acsenergylett.7b01346. eprint:
       https://doi.org/10.1021/acsenergylett.7b01346. URL: https://doi.
       org/10.1021/acsenergylett.7b01346.

[45]   UKPower. URL: https://www.ukpower.co.uk/home_energy/tariffs-per-
       unit-kwh#:~:text=The%20unit%20rate%20you%20pay,per%20kWh%20is%203.
       80p.. (accessed: 23/08/2020).

[46]   Daniel M. Kroupa et al. "Quantum-Cutting Ytterbium-Doped CsPb(Cl1−xBrx)3
       Perovskite Thin Films with Photoluminescence Quantum Yields over 190%".
       In: *ACS Energy Letters* 3.10 (2018), pp. 2390–2395. DOI: 10.1021/acsenergylett.
       8b01528.